Vietnam Journal of Earth Sciences, 47(1), 16-41, https://doi.org/10.15625/2615-9783/21539

Vietnam Journal of Earth Sciences
https://vjs.ac.vn/index.php/jse

Pleistocene basaltic volcanism in the southeastern Ailao Shan - Red River Shear zone: Implications for the injection of metasomatized asthenospheric mantle under the region

Nguyen Hoang[1], Ryuichi Shinjo[2,3], Le Duc Luong*[1], Tran Thi Huong[1], Tran Viet Anh[1], Phan Dong Pha[4], Pham Thanh Dang[1], Cu Sy Thang[1], Nguyen Thi Thu[1], Le Thi Phuong Dung[1]

[1]*Institute of Geological Sciences, VAST, Hanoi, Vietnam*
[2]*Research Institute for Humanity and Nature (RIHN), Motoyama 457-4, Kamigamo, Kita-ku, Kyoto 603-8047, Japan*
[3]*Department of Physics and Earth Sciences, University of the Ryukyus, Senbaru-1, Nishihara, Okinawa 903-0213, Japan*
[4]*Institute of Marine Geology and Geophysics, VAST, Hanoi, Vietnam*

Received 05 July 2024; Received in revised form 06 August 2024; Accepted 16 September 2024

ABSTRACT

The Lung Po basalt, dating to 0.93, 0.81, and 0.47 Ma, occupies approximately 1 km² and is situated 12 km west of the Ailao Shan Red River Shear Zone (ASRRSZ) and about 65 km south of the 12-0 Ma Maguan intraplate volcanic area in southwest Yunnan (SW China), within the ASRRSZ. This olivine-bearing phyric alkaline basalt is characterized by high TiO_2 (around 2.3 wt.%), MgO (8-10 wt.%), and K_2O (approximately 2.8-3 wt.%) with Na_2O/K_2O ratios ranging from 1 to 1.2. These features partially overlap with the Maguan mantle xenolith-bearing alkaline basalt but are distinct from the Pleistocene alkaline basalt of Vietnam's Western Highlands. The Lung Po basalts exhibit a typical oceanic island basalt (OIB) trace element distribution pattern and a 'crossing' rare earth element (REE) pattern, indicating magma generation possibly by melting of garnet peridotite. They have high $^{87}Sr/^{86}Sr$ isotopic ratios (around 0.706) and low $^{143}Nd/^{144}Nd$ ratios (approximately 0.5126), along with moderate $^{206}Pb/^{204}Pb$ and $^{176}Hf/^{177}Hf$ isotopic ratios (respectively <18.3-18.4 and 0.28295-0.2830). These isotopic characteristics, coupled with OIB trace element features, challenge the involvement of crustal material. The Lung Po Pleistocene basalt and the 12-0 Ma Maguan alkaline basalt differ significantly from the 42-24 Ma post-collision high-K magmas in the ASRRSZ, which are associated with crustal tectonic processes. Instead, the Lung Po (and Maguan) basalt likely originated from a newly emplaced, metasomatically altered fertile asthenosphere following localized lithosphere extension and delamination after the India-Eurasian collision events.

Keywords: Lung Po, India-Eurasian collision, post-collision magmatism, metasomatized asthenosphere, recycled sediment.

1. Introduction

The Ailao Shan-Red River Shear Zone (ASRRSZ), proposed by Tapponnier et al. (1982, 1990), resulted from the collision between the Indian and Eurasian plates, driving the spreading and formation of the East Vietnam Sea (also known as the South China Sea, after that EVS/SCS). Despite its critical role in regional tectonic, magmatic,

*Corresponding author, Email: leducluong@igsvn.vast.vn

and mineralogical models, the evolutionary history of the ASRRSZ remains debated (Briais et al., 1993; Harrison et al., 1996; Chung et al., 1997; Leloup et al., 2001).

The ASRRSZ extends over 1000 km from Tibet to the EVS/SCS and contains four metamorphic blocks with varying grades, reaching granulite facies in regions like the Day Nui Con Voi in Vietnam and Ailao Shan, Diancang Shan, and Xuelong Shan in China. Recent isotopic dating indicates that the metamorphic rocks in the Red River zone formed during the Late Oligocene to Early Miocene (Harrison et al., 1996; Wang et al., 1998; Tapponnier et al., 1990; Leloup et al., 2001). Debates concern the timing of shear zone formation, its development stages, and the heat source for high-temperature metamorphism (Leloup et al., 2001). Maluski et al., 2001) identified two phases of tectonic activation and uplift: an early Oligocene phase (37-35 Ma) and a primary movement phase of the Red River zone (25-21 Ma).

The ASRRSZ's tectonic activity is believed to have four main stages: initial spreading (~60-40 Ma), tectonic compression (~40-23 Ma), continued compression and folding (~23-5 Ma), and ongoing faulting from ~5 Ma to present. These stages are accompanied by magmatic activity, indicating that the displacement of the Red River zone impacts both the lithospheric crust and upper mantle (Zhang and Schärer, 1999; Wang et al., 2001; Guo et al., 2006).

High-potassium volcanic rocks erupted between 42-24 Ma in the northern and northwestern parts of the Ailao Shan-Red River fault zone, with younger, scarce intraplate-type basalt eruptions (12-0 Ma) in western Yunnan (Wang et al., 2001; Flower et al., 2013; Liu et al., 2014; Zhang et al., 2017; Xie et al., 2021). In Vietnam, the ASRRSZ includes mafic and ultramafic assemblages such as peridotite, pyroxenite, and gabbro discovered between Yen Bai and Lao Cai, aged 35 and 25 million years, coinciding with periods of thermobaric metamorphism and left-lateral strike-slip movement (Tran et al., 2016). Granite associations aged 35-22 million years are common in the Red River zone (Pham et al., 2022).

Miocene-Quaternary volcanic rocks are sparse in northern Vietnam. Notable exposures include 4.8 Ma basalt and andesite-basalt in the Dien Bien Phu airport area, associated local pull-apart spreading and subsidence processes (Koszowska et al., 2007). Additionally, 3.5-4.5 Ma sub-alkaline and alkaline basalt are found in the Nghia Dan District of western Vietnam (Hoang et al., 2014; Huong and Hoang, 2018). The Lung Po outcrop, located along the Vietnam and China border, consists of dark gray to black basalt forming boulders or five-sided columns. This basalt block, covering approximately 1 km^2, lies about 12 km west of the ASRR Shear zone, around 60 km from the Maguan basalt area and 75 km to the Gejiu basalt area in western Yunnan (Wang et al., 2001; Xie et al., 2021) (Fig. 1). The latter is characterized by asthenosphere-derived K-rich basalts and basanites, enriched in high-field strength elements (HFSE) and large ionic lithophile elements (LILE), similar to regional East and Southeast Asian Neogene-Quaternary basalts (e.g., Flower et al., 2013; Xie et al., 2021). Given these geochemical features and their proximity to the Lung Po outcrop, key questions arisen: Were the Lung Po magmas produced in a heterogeneous asthenosphere or the continental lithospheric mantle? What role did the ASRRSZ activity and the mantle responses to the India-Eurasia collision play in this magmatism?

To address the above questions, Lung Po basalt samples were collected to analyze eruption age, elemental geochemical composition, and Sr, Nd, Pb, and Hf isotopes.

The data were interpreted to determine the P-T conditions of primitive melt generation, the characteristics of source enrichment or depletion, and its origin, consistent with local seismic data. This analysis proposes a magma generation model corresponding to the ASRRSZ activities following the India-Eurasian collision.

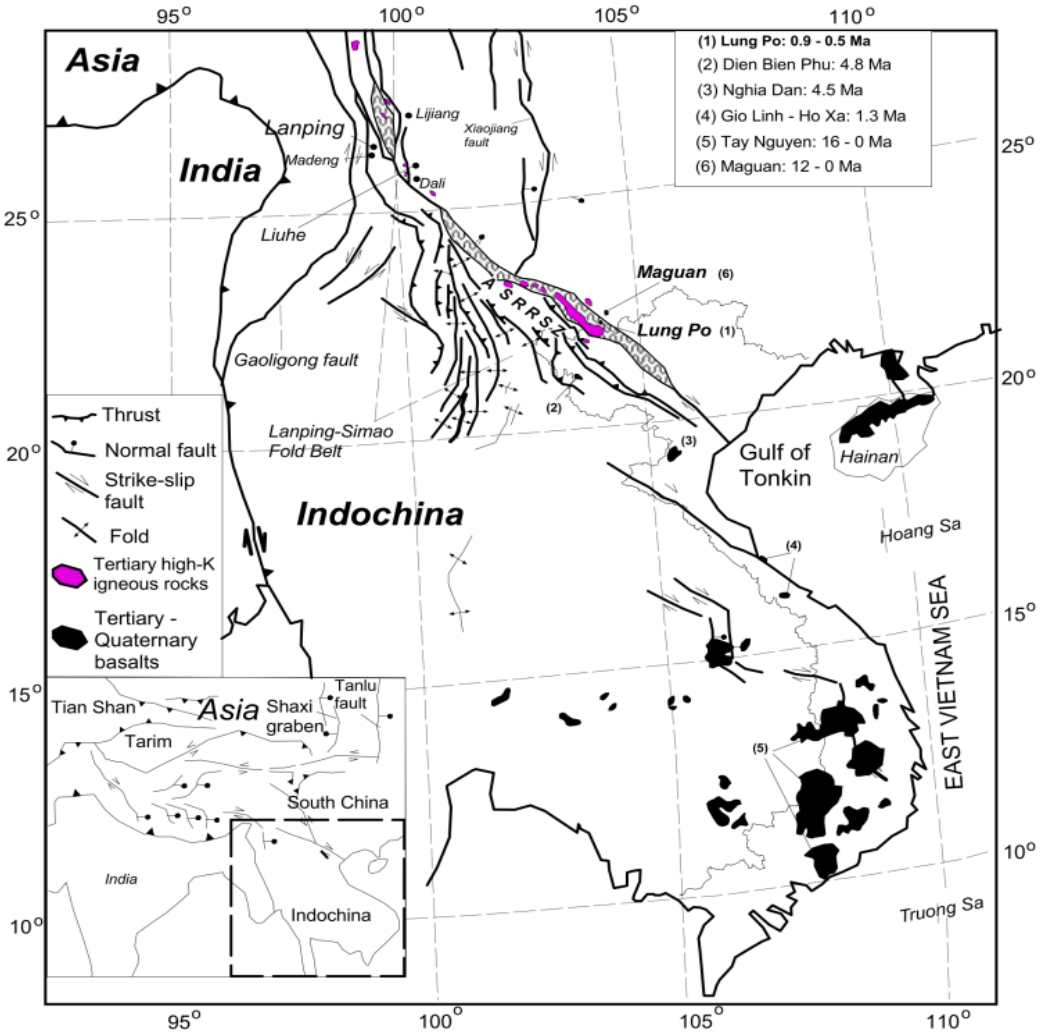

Figure 1. The scheme of India-Eurasian collision and distribution scheme of post-collision volcanism and regional faults in China and Vietnam are simplified after Wang et al. (2001) and Hoang and Flower (1998). The ages of Maguan basalts are from Wang et al. (2001) and Xie et al. (2021); the Lung Po basalts' ages are from this study; other Vietnamese basalts are from Hoang and Flower (1998). ASRRSZ: Ailao Shan Red River Shear Zone

2. Petrography

The Lung Po basalt outcrop is located at coordinates 22°43'34"N and 103°34'58"E, situated between the A Lu and Y Ty communes at the northernmost tip of Bat Xat district, Lao Cai province, on the right bank of the Red River, along the Vietnam-China border. The outcrop covers approximately (length, width, and height)

300 × 250 × 70-100 m) overlying Permian-Triassic granitoid rocks. It forms a sedimentary-volcaniclastic layer composed of gravel, tuff, lava fragments (bombs), and reddish-brown volcanic ash, which can be several meters thick. The basalt occurs as blocks up to 2 × 2 × 1 m in size or as 4- to 5-sided columns with diameters less than 0.4 m. The outcrop is visible from the bottom of Lung Po Creek (which delineates the border between Vietnam and China) to the top, appearing almost monolithic and making it difficult to distinguish individual lava flows. However, citing the eruption ages (see below), several eruption episodes must have formed the outcrop. At the top of the outcrop, to the west, at an altitude of 510 m (sample LPO-10), about 70 meters higher than the first sampling site (LPO-1) along the border, the basalt appears as smaller blocks, showing evidence of tectonic compression fractures.

Lung Po basalt is phyric, with olivine being the only phenocryst taking up to 15 vol.% of the rock. The phenocrysts are lemon yellow, usually euhedral or subhedral, with various sizes from 0.1 by 0.2 to 1 by 2 mm, with high interference color and high forsteritic content. Olivine irregularly spreads on the plagioclase microlitic or glassy groundmass, containing a large amount of Fe-Ti oxide. Sometimes encountered are olivine aggregates (Fig. 2), which may be products of fractional crystallization of earlier melt factions. Sometimes, large (2 by 5 mm), fresh ortho- or clinopyroxene xenocryst fragments are also encountered, which usually form thermo-chemical reaction rims with the basaltic groundmass.

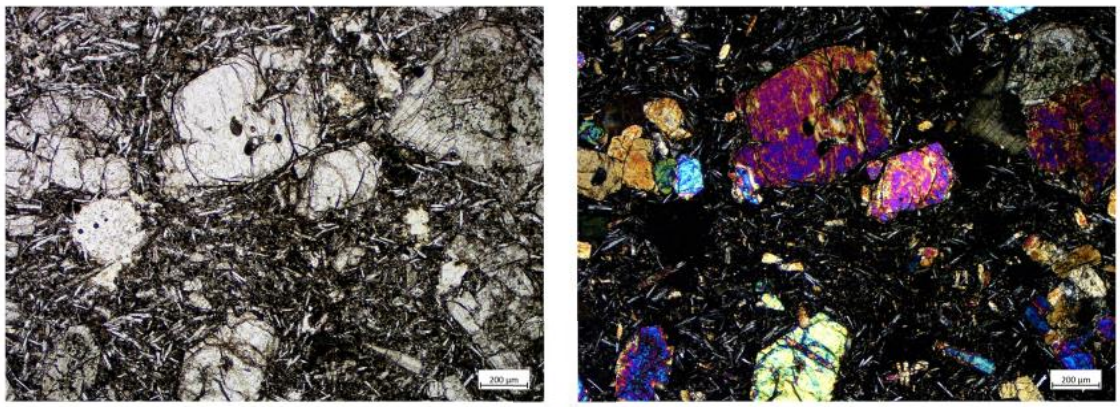

Figure 2. A photomicrograph of a representative Lung Po Pleistocene alkaline basalt shows euhedral and subhedral olivine phenocrysts on a holohyaline groundmass with plagioclase microlite and Fe-Ti oxides; the left photo is taken under plain light, and the right photo is taken under polarized light

3. Analytical procedures

3.1. K-Ar age dating

Samples were processed and analyzed for K-Ar age data at the K/Ar laboratory, Institute of Nuclear Research, Hungarian Academy of Sciences (ATOMKI Debrecen, Hungary). Details of the analytical method are given in Balogh (1985) and Balogh et al. (1986) but briefly described as follows:

Determination of potassium concentration: Approximately 50 mg of finely ground samples were digested in a mixture of concentrated HNO_3 and HF acids within Teflon beakers. Following evaporation, the samples were dissolved in 0.2 M HCl.

Potassium concentrations were determined using flame photometry, with a sodium buffer and lithium as an internal standard, employing an Industrial M420 type flame photometer. Multiple runs of inter-laboratory standards (Asia1/95, LP-6, HD-B1, Gl-0) confirmed the method's accuracy and reproducibility, maintaining a deviation within 2%.

Argon measurements: Approximately 0.5 g of samples were wrapped in aluminum foil and copper sieves, then preheated for about 24 hours at 150-180°C under vacuum. Argon was extracted under ultra-high vacuum conditions via RF induction heating and fusion of rock samples in molybdenum crucibles. The gas was purified using a titanium sponge and SAES St 797 type getters to remove chemically active contaminants and a cold trap containing liquid nitrogen. The extraction line was directly connected to a mass spectrometer (90° magnetic sector type with a 155 mm radius, equipped with a Faraday cup, built at ATOMKI, Debrecen, Hungary) operating in static mode. Argon isotope ratios were measured using a 38Ar isotope dilution mass spectrometric method, calibrated with atmospheric argon and international rock standards. Experimental details of the K/Ar dating method used at ATOMKI Debrecen and calibration results were provided by Balogh (1985). The age of the samples was calculated using the decay constants recommended by Steiger and Jäger (1977). Analytical errors are reported at a 60% confidence level (1σ), following the equation provided by Cox and Dalrymple (1967).

3.2. Major element composition analysis

The analysis was conducted at the Faculty of Physics and Earth Sciences, University of the Ryukyus (Okinawa, Japan), using a ZSX Primus II XRF mass spectrometer on glass beads. During the analytical process, the Geological Survey of Japan and the U.S. Geological Survey (USGS) 's geological standards, such as JA-1, JA-2, JB-1, JB-1a, JB-3, JR-1, JP-1, BCR-2, and BHVO-2 were used to construct calibration lines and to evaluate the precision and accuracy of the data. The silicate oxides' analytical error (1σ) varies from ±1 to ±2% (Table 1).

3.3. Trace element composition analysis

For the analysis, about 50 mg of powdered samples were weighed in a 15 ml Teflon beaker for trace element composition using a Thermo Scientific Element 2 Q-ICP-MS at the Faculty of Physics and Earth Sciences, University of the Ryukyus, Okinawa, Japan. Samples were dissolved in mixtures of concentrated HNO_3 and HF acids by the ratio of 1:2 and then left on a hotplate at 135°C for at least 48 hours in the ISO 5 metal-free chemical clean laboratory at the Institute of Geological Sciences, Vietnam Academy of Science and Technology (VAST). The samples were evaporated till complete dryness, then dissolved in 1 ml of 15N HNO_3, repeated twice to allow the samples to dissolve completely. The samples were then evaporated to dryness. To eliminate possible CaF_2 residue as a result of CaO and HF interaction during dissolution, add 1 ml of 12N (37%) HCl to dry and warn samples, cap, and leave on a hotplate at about 60°C for about 30 minutes, then add 5 ml of milli-Q and evaporate to complete dryness. Add 3 ml of 2N HNO_3 (about 3.3 grams), cap, and leave on a hotplate at low temperature overnight to allow proper equilibrium. Weigh about 0.164 grams of the solution in about 10 ml of 0.3N HNO_3 to dilute the sample to 4000 ± 0.0005 times for mass spectrometry analysis. During the analysis, JA-1, JB-1a, BHVO-2, and BCR-2, the Geological Survey of Japan (GSJ), and USGS' geological standards were repeatedly analyzed to verify the precision and accuracy of the data. The trace element compositions and their corresponding ±2σ errors are given in Table 1.

Table 1. Ages, geochemical and Sr-Nd-Hf-Pb isotopic compositions of the Lung Po basalts

Sample	LPO-1	LPO-2	LPO-3	LPO-4	LPO-5	LPO-6	LPO-7	LPO-8	LPO-9	LPO-10	JB-1a (†)	JB-1a (‡)	±σ (n=3)
Coordi-nates	22°43'38.9"	22°43'37.21"	22°43'37.45"	22°43'37.47"	22°43'37.48.5"	22°43'17.24"	22°43'17.25"	22°43'18"	22°43'18"	22°43'18"			
	103°34'52.4"	103°34'51"	103°34'48"	103°34'41.2"	103°34'40.5"	103°34'40"	103°34'39.4"	103°34'39"	103°34'38.2"	103°34'38.1"			
Elevation	440 m	440 m	440 m	440 m	445 m	445 m	445 m	500 m	505 m	510 m			
K/Ar age (m.y)			0.81 ±0.22				0.93 ±0.20		0.47±0.14				
SiO_2	49.54	50.30	49.18	47.61	47.64	49.74	47.93	47.98	50.25	47.54	51.01	52.41	0.65
TiO_2	2.30	2.26	2.34	2.34	2.33	2.32	2.29	2.25	2.25	2.30	1.27	1.28	0.02
Al_2O_3	12.20	12.49	12.85	12.47	12.34	12.29	12.42	12.18	12.24	12.27	13.93	14.45	0.09
Fe_2O_3T	10.74	10.74	11.38	11.11	11.08	10.79	11.04	10.61	10.50	10.87	8.76	8.33	0.43
MnO	0.15	0.16	0.16	0.16	0.16	0.15	0.16	0.16	0.14	0.16	0.14	0.15	0.00
MgO	9.27	7.93	8.67	8.94	8.92	9.53	9.05	9.79	9.16	8.97	7.67	7.83	0.08
CaO	8.52	7.99	8.64	9.57	9.54	8.49	9.52	9.16	7.92	9.41	9.09	9.31	0.09
Na_2O	2.93	3.13	3.22	3.28	3.10	2.98	3.38	2.56	3.06	2.91	2.85	2.73	0.05
K_2O	2.76	2.84	2.96	2.88	2.90	2.78	2.84	2.82	2.71	2.76	1.38	1.40	0.02
P_2O_5	0.51	0.50	0.53	0.59	0.59	0.52	0.59	0.55	0.48	0.56	0.25	0.26	0.01
LOI	0.98	1.05	0.00	0.97	1.10	0.00	0.67	1.13	1.02	0.95	3.56	1.84	
Total	99.90	99.39	99.93	99.93	99.70	99.60	99.90	99.20	99.73	98.71	99.90	99.99	
Mg#	64.4	60.8	61.5	62.8	62.8	65.0	63.2	65.9	64.7	63.4			
Li	9.8	8.2	9.2	8.4	7.1	9.2	9.3	0.4	4.0	10.8	10.9	11.44	4.7
Be	1.6	1.8	1.6	1.8	1.8	1.5	1.8	0.1	0.5	1.8	1.44	1.42	1.8
Sc	13.9	13.7	12.6	13.6	13.5	12.7	17.9	0.7	6.8	20.8	27.9	28.11	0.8
V	213.4	202.2	199.1	245.4	242.3	214.3	245.5	138.5	129.5	215.4	205	214.61	4.5
Cr	299.5	270.9	276.3	218.6	222.6	486.7	219.1	251.4	326.2	226.6	392	403.36	2.8
Co	55.3	56.3	54.7	52.9	52.0	57.5	50.9	52.3	53.0	50.0	38.6	38.41	0.5
Ni	241.0	371.0	352.3	189.3	189.3	248.5	164.8	216.2	268.2	199.5	139	136.91	1.5
Cu	78.6	155.2	149.5	78.5	75.3	86.5	69.2	76.9	91.2	78.7	56.7	56.87	0.3
Zn	123.7	119.8	129.1	118.5	116.2	127.1	122.2	118.4	127.1	116.9	82.1	90.33	9.1
As	0.65	0.54	0.65	0.96	0.84	0.75	0.74	1.08	0.07	0.61			
Rb	41.2	45.0	44.2	56.2	104.6	42.9	71.6	63.4	87.2	99.8	39.2	39.32	0.3
Sr	522.7	474.8	494.4	629.7	579.0	521.9	651.4	606.2	573.4	667.8	442	447.67	1.3
Y	22.5	26.9	22.4	24.1	23.0	23.8	25.8	25.0	27.7	27.7	24	24.01	0
Zr	205.3	196.3	195.9	209.2	202.2	220.4	214.5	223.5	223.9	212.7	144	140.89	2.2
Nb	53.4	49.0	48.4	63.5	62.7	55.3	63.3	58.4	52.6	59.2	26.9	28.75	6.4
Mo	1.64	2.03	1.98	3.30	3.25	2.48	3.19	3.58	1.24	2.87	1.57	1.62	2.8
Cd	0.14	0.15	0.13	0.14	0.13	0.15	0.14	0.15	0.14	0.16	0.1	0.09	1.4
Sn	2.52	2.53	2.49	2.40	2.40	2.64	2.39	2.63	2.91	2.55	-	-	-
Cs	0.19	0.15	0.11	0.31	0.29	0.20	0.47	0.60	0.44	0.97	1.31	1.26	3.8
Ba	610.8	662.8	614.4	827.0	895.1	646.7	902.9	745.6	633.0	811.3	504	501.80	0.4
La	25.27	30.74	27.03	34.79	33.82	26.38	36.69	32.73	27.47	35.41	37.6	37.80	0.5
Ce	52.41	52.98	55.59	69.78	67.94	55.26	71.82	65.39	53.99	70.05	65.9	66.91	1.5
Pr	6.68	7.59	7.10	8.49	8.30	7.02	8.68	8.17	7.32	8.64	7.3	6.95	5
Nd	28.03	31.31	29.36	33.51	32.95	29.06	34.32	33.17	31.10	34.85	26	26.32	1.2
Sm	6.57	7.24	6.73	7.25	7.14	6.93	7.35	7.41	7.60	7.73	5.07	5.01	1.1
Eu	1.90	2.07	1.91	2.08	2.04	2.00	2.12	2.14	2.19	2.27	1.46	1.48	1.5
Gd	5.55	6.26	5.77	6.11	5.98	5.88	6.19	6.28	6.43	6.51	4.67	4.74	1.5
Tb	0.78	0.88	0.80	0.83	0.82	0.82	0.84	0.88	0.94	0.92	0.69	0.71	3.3
Dy	4.04	4.56	4.07	4.24	4.16	4.24	4.33	4.71	5.04	4.91	3.99	4.17	4.4
Ho	0.64	0.72	0.65	0.68	0.67	0.67	0.70	0.77	0.80	0.79	0.71	0.83	14.1
Er	1.75	1.97	1.74	1.89	1.83	1.82	1.96	2.13	2.25	2.27	2.18	2.25	3.2
Tm	0.24	0.26	0.24	0.26	0.25	0.25	0.27	0.30	0.31	0.31	0.33	0.33	1.6
Yb	1.42	1.57	1.41	1.56	1.53	1.50	1.64	1.79	1.85	1.92	2.1	2.08	0.8
Lu	0.21	0.23	0.21	0.23	0.22	0.22	0.24	0.27	0.27	0.29	0.33	0.31	6.4
Hf	3.93	3.91	3.83	3.92	3.87	4.08	3.91	4.62	4.90	4.68	3.41	3.52	3.2
Ta	3.01	2.82	2.75	3.49	3.45	3.13	3.44	3.67	3.36	3.78	1.93	1.90	1.8
W	0.52	0.60	0.34	0.98	1.05	0.66	0.92	1.12	0.26	0.96	-	-	-
Pb	3.09	3.26	3.30	3.19	3.16	2.98	3.60	4.23	3.71	4.23	6.76	6.60	2.4
Th	2.63	2.56	2.49	3.49	3.30	2.59	3.92	4.18	3.59	4.81	9.03	9.15	1.3
U	0.77	0.64	0.75	0.82	0.78	0.72	0.78	0.88	0.71	0.83	1.57	1.61	2.7

(†) The Geological Survey of Japan's recommended values; (‡) this study's analysis

Table 1 (continued)

Sample	LPO-1	LPO-2	LPO-3	LPO-4	LPO-5	LPO-6	LPO-7	LPO-8	LPO-9	LPO-10
$^{87}Sr/^{86}Sr$	0.706033	0.706388	0.706383	0.70588	0.706057	0.705999	0.706272	0.706077	0.705974	0.705910
±2σ	0.00002	0.00001	0.00002	0.00002	0.00003	0.00002	0.00002	0.00002	0.00002	0.00002
$^{87}Sr/^{86}Sr$*	0.706023	0.706388	0.706428	0.705893	0.706057	0.706006	0.706236	0.706099	0.705995	0.705914
±2σ	0.000008	0.000009	0.000007	0.000007	0.000009	0.000007	0.000009	0.000009	0.000010	0.000008
$^{143}Nd/^{144}Nd$	0.512645	0.512627	0.512593	0.512644	0.51263	0.512621	0.512593	0.512565	0.512644	0.512627
±2σ	0.000011	0.000011	0.000010	0.000009	0.000009	0.000010	0.000007	0.000011	0.000011	0.000013
ε_{Nd}	0.14	-0.21	-0.88	0.12	-0.16	-0.33	-0.88	-1.42	0.12	-0.21
$^{143}Nd/^{144}Nd$*	0.512634	0.512609	0.51259	0.512636	0.512623	0.512628	0.51261	0.512586	0.512652	0.512631
±2σ	0.000007	0.000007	0.000008	0.000008	0.000007	0.000009	0.000007	0.000008	0.000008	0.000007
ε_{Nd}*	0.14	-0.21	-0.88	0.12	-0.16	-0.33	-0.88	-1.42	0.12	-0.21
$^{206}Pb/^{204}Pb$	18.4051	18.4043	18.4145	18.3351	18.3127	18.4091	18.3440	18.4125	18.4003	18.3403
±2σ	0.0004	0.0004	0.0003	0.0004	0.0005	0.0003	0.0004	0.0005	0.0006	0.0004

Sample	LPO-1	LPO-2	LPO-3	LPO-4	LPO-5	LPO-6	LPO-7	LPO-8	LPO-9	LPO-10
$^{206}Pb/^{204}Pb$*	18.412	18.411	18.421	18.342	18.319	18.416	18.351	18.396	18.408	18.337
±2σ	0.0004	0.0004	0.0003	0.0004	0.0005	0.0003	0.0004	0.0003	0.0004	0.0005
$^{207}Pb/^{204}Pb$	15.6296	15.6406	15.6387	15.6279	15.6266	15.6348	15.6323	15.6285	15.6196	15.6201
±2σ	0.0005	0.0005	0.0004	0.0005	0.0005	0.0005	0.0005	0.0005	0.0006	0.0004
$^{207}Pb/^{204}Pb$*	15.6239	15.6327	15.6301	15.6170	15.6161	15.6219	15.6207	15.6285	15.6196	15.6201
±2σ	0.0003	0.0003	0.0003	0.0004	0.0005	0.0002	0.0004	0.0005	0.0006	0.0004
$^{208}Pb/^{204}Pb$	38.8067	38.9089	38.9223	38.8391	38.8212	38.9335	38.8743	38.9238	38.8418	38.8466
±2σ	0.0014	0.0013	0.0013	0.0015	0.0015	0.0014	0.0013	0.0017	0.0017	0.0011
$^{208}Pb/^{204}Pb$*	38.8547	38.8825	38.8878	38.7885	38.7753	38.8737	38.8304	38.9238	38.8418	38.8466
±2σ	0.0008	0.0009	0.0007	0.0009	0.0011	0.0007	0.0011	0.00112	0.0011	0.0007
$^{176}Hf/^{177}Hf$*	0.282993	0.283008	0.282974	0.282948	0.283025	0.282988	0.282918	-	-	0.283049
±2σ	0.000004	0.000003	0.000004	0.000003	0.000003	0.000003	0.000004			0.000006
ε_{Hf}*	7.34	7.89	6.69	5.76	8.49	7.19	4.70			9.34

(*) Data acquired at the Institute of Geological Sciences, VAST, using a NU Plasma 3 MC-ICP-MS;
$\varepsilon_{Hf} = [(^{176}Hf/^{177}Hf_{sample})/(^{176}Hf/^{177}Hf_{CHUR})-1]*10^4$, where $^{176}Hf/^{177}Hf_{CHUR}$ (Chondrite Uniform Reservoir) = 0.28278 (after Bouvier et al., 2008); $\varepsilon_{Nd} = [(^{143}Nd/^{144}Nd_{sample})/(^{143}Nd/^{144}Nd_{CHUR})-1]*10^4$, where $^{143}Nd/^{144}Nd_{CHUR}$ = 0.512638 (after DePaolo and Wasserburg, 1976)

3.4. Sr, Nd, Hf, and Pb isotopic composition analysis

For the analysis, about 60 mg of sample were weighed in 15 ml Teflon beakers, added ultra-clean, concentrated HNO_3 and HF acids at a 1:2 ratio, and placed on a hotplate at about 135°C for at least 48 hours. After evaporation, 1 ml of concentrated HNO_3 acid was added and evaporated repeatedly to ensure the samples were dissolved completely. About 15-20 mg of dissolved samples were used for elemental extraction. Sr and Pb were extracted by ca. 50 µl Eichrom Sr-spec resin in 1 ml quartz tubes as columns, using diluted HNO_3 and strong HCl acids, respectively, as eluants. Nd and Hf were extracted in 1 ml Eichrom Ln resin bed in 10 ml quartz columns, using, respectively, diluted HCl and weak HF-HCl mixture as eluant (Shinjo et al., 2010; Hoang et al., 2019). Isotope ratios $^{87}Sr/^{86}Sr$, $^{143}Nd/^{144}Nd$, $^{206}Pb/^{204}Pb$, $^{207}Pb/^{204}Pb$, and $^{208}Pb/^{204}Pb$ were analyzed at the Faculty of Physics and Earth Sciences, University of the Ryukyus, Okinawa, Japan, using a Neptune Plus MC-ICP-MS. another set of Lung Po samples were re-analyzed for isotopic data, including $^{176}Hf/^{177}Hf$ isotopic ratios, at the Institute of Geological Sciences, VAST, using a NU Plasma 3 MC-ICP-MS for data accuracy verification. During the lead isotopic analysis, thallium (Tl) was added to the lead solution at about 1:8 for internal mass-fractionation correction, and NIST981, a lead standard, was embedded between samples throughout the analytical process. This standard was used for accuracy verification and data correction. The lead data were reported relative to $^{206}Pb/^{204}Pb$, $^{207}Pb/^{204}Pb$, and $^{208}Pb/^{204}Pb$ of NBS981 at 16.938 ±0.0006, 15.493 ±0.0005, and 36.704 ±0.0016, respectively. Strontium fractionation was corrected to $^{86}Sr/^{88}Sr$ =0.1194, and data were reported relative to $^{87}Sr/^{86}Sr$ = 0.710255 for the NBS987 standard. During the analysis, the strontium running procedure was programmed to minimize the interference of ^{84}Kr and ^{85}Rb to the data reliability and accuracy. The $^{143}Nd/^{144}Nd$ data were fractionation corrected to $^{146}Nd/^{144}Nd$ = 0.7219 and reported relative to a value of $^{143}Nd/^{144}Nd$ = 0.512115 for the Geological Survey of Japan JNdi-1 neodymium standard. The value of $^{176}Hf/^{177}Hf$ of JMC475, a hafnium isotopic standard, showed 0.282136 and was used for data correction (e.g., Wiedenbeck et al., 1995). Data are shown in Table 1.

4. Analytical results

4.1. Major element compositions

Lung Po basalts, aged from about 0.93 to 0.47 Ma, are classified as alkali basalt or trachy-basalt in the TAS (total alkali - SiO_2) diagram of Le Bas et al. (1986) (Fig. 3). They have medium SiO_2 concentration, from 47.5

to 50.5 (wt.%) with $Na_2O + K_2O$ ranging from about 5 to 6 and Na_2O/K_2O being about 1. Compared to 12-0 Ma basalts from the Maguan and nearby areas (e.g., Wang et al., 2001; Flower et al., 2013), about 60-80 km north, Lung Po basalts' total alkaline contents are much lower, although their SiO_2 concentrations are about similar. Lung Po magmas have higher SiO_2 contents and slightly higher total alkaline oxides than contemporaneous, representative alkaline basalts from Vietnam Western Highlands (Hoang et al., 2019).

Lung Po basalts are relatively magnesian, with MgO ranging from 8 to 10 (wt.%), partially overlapping some of the 12-0 Ma Maguan samples, and are about in the same range as Vietnam Western Highlands' alkaline basalts (Fig. 4). Other post-collision magmas such as high-K rocks from northern (Guo et al., 2006) and southwestern Tibet (Liu et al., 2014), and 42-24 Ma Dali-Lijiang (western Yunnan) (Wang et al., 2001; Flower et al., 2013), having MgO from ca. 9 to 1 (wt.%) corresponding to a SiO_2 range from ca. 45 to 72 (wt.%), show negative correlation between MgO and SiO_2, suggesting fractional crystallization and the involvement of crustal material in their formation and evolution is significant (e.g., Guo et al., 2006; Wang et al., 2001; Liu et al., 2014; Zhang et al., 2017).

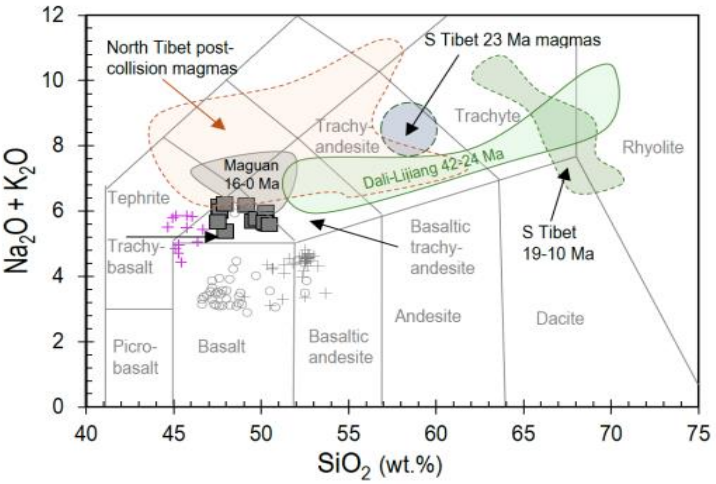

Figure 3. Na_2O+K_2O vs. SiO_2 (TAS) classification diagram for the Lung Po basalts (filled square) (e.g., Le Bas et al., 1986), plotted are Vietnam's Western Highlands Pleistocene tholeiite (gray cross) and alkaline basalt (pink cross; Hoang et al., 2019), and SE I-MORB (empty circle; Neal et al., 2002); also plotted for reference are data field of North Tibet 42-24 Ma high-K magmas (Guo et al., 2006), South Tibet 23 and 19-10 Ma magmas (Liu et al., 2014), and Dali-Lijiang 42-24 high-K magmas and Maguan 12-0 Ma basalts (after Wang et al., 2001)

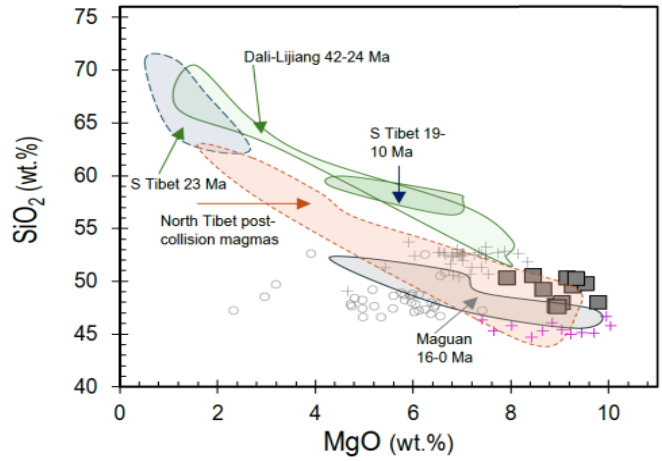

Figure 4. Lung Po basalts with high MgO (wt.%) and relatively low SiO_2 (wt.%) partially overlap the Maguan 12-0 Ma basalts and a few samples from North Tibet post-collision high-K mafic rocks. Sources of reference data fields are as in Fig. 3

4.2. Trace element compositions

The distribution curve of trace element-normalization to the primitive mantle of the Lung Po basalts is of oceanic island basalt (OIB) type (after Sun and McDonough, 1989) (Fig. 5a) except a minor peak at Pb and a trough at Th and U. The chondrite rare earth element normalization configuration is OIB-like with light rare earth element (LREE) smoothly descending to heavy (H) REE (Fig. 5b) with a Lung Po basalts' La/Yb ratio average ca. 20 compared to the North Arch (Hawaii Islands) mantle plume-related alkaline basalts at 19.5 (Frey et al., 2000) and an average of representative alkaline basalts from Vietnam Western Highlands at 24 (Hoang et al., 2019).

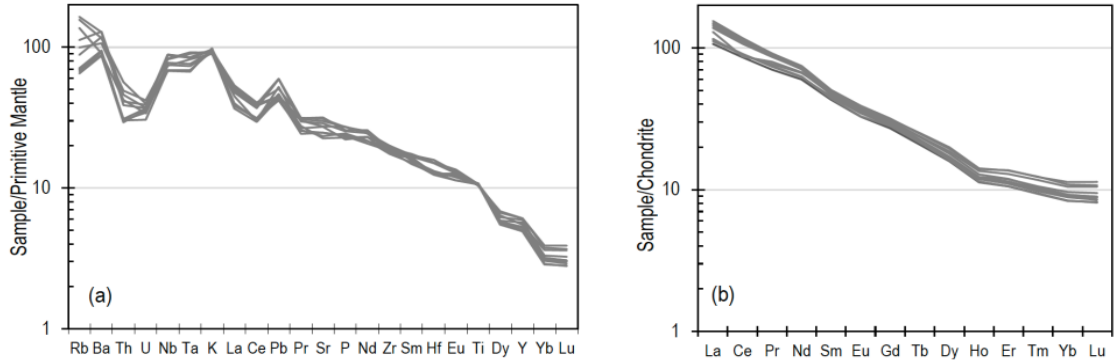

Figure 5. (a) The primitive mantle trace element normalization patterns for the Lung Po basalts, except for the Th and U troughs, are essentially oceanic island basalt-type (normalizing data are from Sun and McDonough, 1989); (b) The chondrite rare earth element (REE) normalization configuration of the Lung Po basalts shows a sharp decrease from the light (L)-REE to middle (M-) and heavy (H-) REE, reflecting a significant depletion of HREE relative to LREE (after Sun and McDonough, 1989)

4.3. Sr-Nd-Hf-Pb isotopic compositions

4.3.1. Plots of $^{87}Sr/^{86}Sr$ vs. ε_{Nd}

The strontium isotopic ratios ($^{87}Sr/^{86}Sr$) of the Lung Po basalts are high, from 0.706 to 0.7065, coupling with low $^{143}Nd/^{144}Nd$ (expressed as ε_{Nd}), plotting in the enriched mantle quadrant (Fig. 6). The high $^{87}Sr/^{86}Sr$ and low $^{143}Nd/^{144}Nd$ isotopic ratios make Lung Po basalts the most isotopically enriched post-collision basalt in Vietnam (Hoang et al., 1996). The 12-0 Ma Maguan basalts (after Wang et al., 2001) plot between southeast Indian Mid-Ocean Ridge Basalt (SE I-MORB) (after Mahoney et al., 2002) and enriched Lung Po basalts, partially overlapping the Western Highlands' alkaline and tholeiitic basalts. Note that the isotopically enriched Lung Po basalts are much 'depleted' relative to north and south, southwest Tibet post-collision, and Dali-Jiang high-K volcanic rocks (after Guo et al., 2006; Liu et al., 2014; Zhang et al., 2017; Wang et al., 2001), which extend to strongly to the field of enriched mantle type 2 (EM2) or continental crust (CC) (e.g., Zindler and Hart, 1986) (see insert in Fig. 6).

4.3.2. Plots of $^{206}Pb/^{204}Pb$ vs. $^{207}Pb/^{204}Pb$ and $^{208}Pb/^{204}Pb$

Lung Po basalts have higher $^{207}Pb/^{204}Pb$ and $^{208}Pb/^{204}Pb$ isotopic ratios at the same $^{206}Pb/^{204}Pb$ ratios than 12-0 Ma Maguan, Vietnam Western Highlands alkaline, and tholeiitic basalts (Table 1). They plot between low-$^{206}Pb/^{204}Pb$ SE I-MORB and high-

$^{206}Pb/^{204}Pb$ Tibet high-K post India-Eurasian collision magmas and above the Northern Hemisphere Reference Line (NHRL, after Hart, 1988) (Fig. 7a-b), while some samples of 12-0 Ma Maguan and Vietnam Western Highlands basalts plot in the SE I-MORB lead isotopic field. The high $^{207}Pb/^{204}Pb$ and $^{208}Pb/^{204}Pb$ relative to $^{206}Pb/^{204}Pb$ isotopic ratios was defined as Dupal anomaly, believed to reside in the Indian ocean mantle (Hart, 1984), although it was reported in East and SE Asian basalt (Tu et al., 1991; Tatsumoto and Nakamura, 1991; Tatsumoto et al., 1992; Hoang et al., 1996).

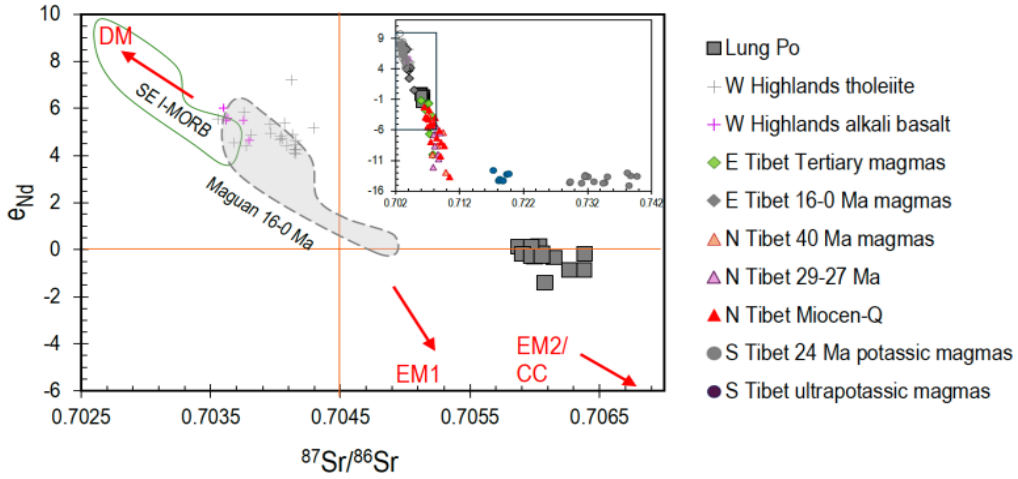

Figure 6. Plots of $^{87}Sr/^{86}Sr$ vs. ε_{Nd} show the Lung Po Pleistocene basalts are much more EM2 enriched than Vietnam's contemporaneous Western Highlands and Maguan basalts; however, they all are much depleted than the Tibet 42-24 Ma high-K magmas (inserted diagram). The SE I-MORB data are from Mahoney et al. (2002). The other sources of data fields are as in Fig. 3. The mantle isotopic components (EM1: enriched mantle type 1, EM2: enriched mantle type 2; DM: depleted mantle) are after Zindler and Hart (1986)

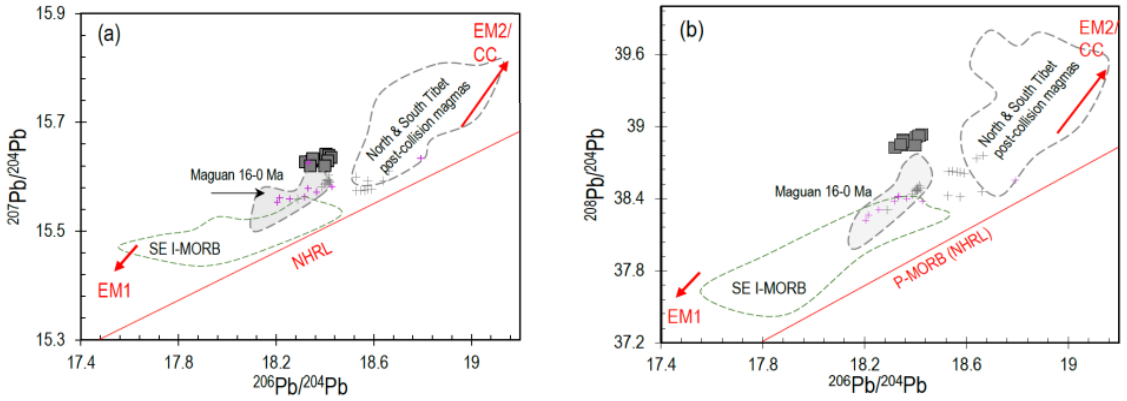

Figure 7. Plots of $^{206}Pb/^{204}Pb$ vs. $^{207}Pb/^{204}Pb$ (a) and $^{206}Pb/^{204}Pb$ vs. $^{208}Pb/^{204}Pb$ (b) show the Lung Po Pleistocene basalts are higher $^{207}Pb/^{204}Pb$ and $^{208}Pb/^{204}Pb$ at the same $^{206}Pb/^{206}Pb$ than other regional contemporaneous basalts. Sources for reference data fields are as in Fig. 2. NHRL (Northern Hemisphere Reference Line) is after Hart (1988) based on Pacific MORB (after White et al., 1987

4.3.3. Plots of ε_{Nd} vs. ε_{Hf}

Plots ε_{Hf} versus ε_{Nd} are shown along with data from south-central Vietnam 6-1 Ma basalts (Richard et al., to be published; Nguyen Hoang unpublished data) (Fig. 8) and data field of the EVS/SCS (after Zhang et al., 2018); these data plot along the terrestrial array. The Lung Po basalts having lower ε_{Nd} values, thus are more enriched relative to the south-central and EVS-MORB basalts; they plot to the left of the terrestrial array line, inclining more toward the field of enriched type 2 (EM2) component.

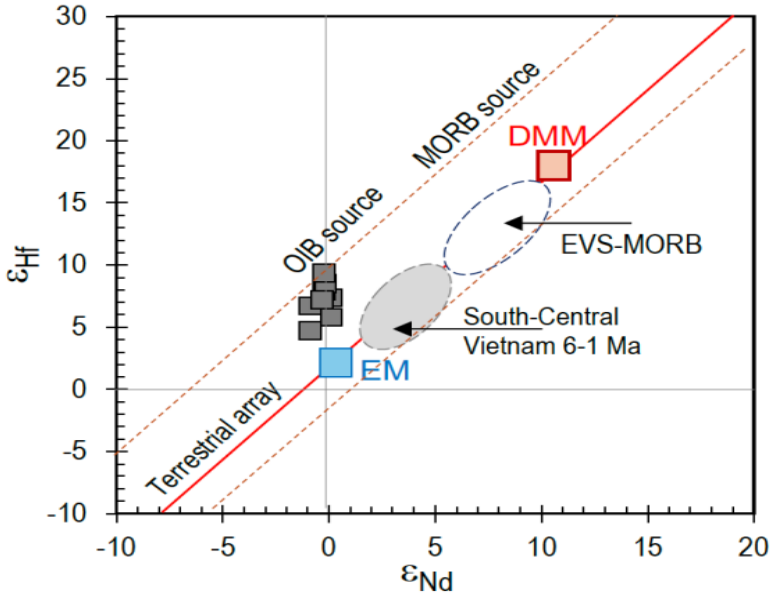

Figure 8. Plots of ε_{Hf} vs. ε_{Nd} show the Lung Po basalts are more enriched in $^{143}Nd/^{144}Nd$ (expressed by ε_{Nd}) relative to $^{176}Hf/^{177}Hf$ (expressed by ε_{Hf}) incline to field of enriched mantle (EM) but in the terrestrial array (modified after Jones et al., 2019). Also plotted are south-central Vietnam 6-1 Ma basalts (Hoang N., unpublished data; Richard et al., to be published) and EVS/SCS mid-ocean-ridge basalt (MORB) (Zhang et al., 2018) for reference

5. Discussions

5.1. Effect of crustal contamination

All Lung Po samples exhibit elevated $^{87}Sr/^{86}Sr$ (reaching up to 0.7064) and depleted $^{143}Nd/^{144}Nd$ ratios (about 0.5126), and notably high $^{206}Pb/^{204}Pb$, $^{207}Pb/^{204}Pb$, and $^{208}Pb/^{204}Pb$ ratios (Figs. 6, 7a-b) are usually considered crustal contamination or interaction with the wall-rock during magmas' passage through the lithosphere. Crustal contamination results in higher concentrations of large-ion lithophile elements such as Ba, Rb, Sr, etc., and high SiO_2 (Rudnick and Fountain, 1995) relative to high-field strength elements such as Nb, Ta, Zr, and Ti (Gill, 1981; McLennan, 2001). The presence of crustal contamination is exhibited by positive correlations observed between $^{87}Sr/^{86}Sr$, $^{206}Pb/^{204}Pb$, $^{207}Pb/^{204}Pb$, and $^{208}Pb/^{204}Pb$ ratios with elements such as SiO_2, Ba, Ba/Nb, Ba/Zr, etc.

Despite having high $^{87}Sr/^{86}Sr$ ratios, Lung Po basalts show low Ba/Nb, ranging from 10 to 14. These values are slightly higher than the primitive mantle (9.7; Sun and McDonough, 1989) but much lower than the

Upper continental crust (UCC) (22; McLennan, 2001), and significantly lower than typical subduction zone magmas (98; Kimura and Yoshida, 2006) (Fig. 9). The Ba/Nb ratios in Lung Po basalts are also considerably lower than those in the post-collision high-K magmas of North and South Tibet and Dali-Lijiang, which range from approximately 50 to 300 and are associated with $^{87}Sr/^{86}Sr$ ratios of 0.708 to 0.740. These higher ratios have been interpreted as evidence of crust contamination or interaction with crustal melts (after Wang et al., 2001; Guo et al., 2006; Flower et al., 2013; Liu et al., 2014; Zhang et al., 2017) (insert in Fig. 9). In summary, the Lung Po basalts, along with nearby Maguan 12-0 Ma magmas, which have Ba/Nb ratios less than 8 and relatively depleted $^{87}Sr/^{86}Sr$ ratios (0.703-0.705), do not appear to be crustally contaminated (Fig. 9). Additionally, plots of ε_{Hf} versus ε_{Nd} align with the terrestrial line, suggesting that these magmas are mantle-derived with minimal influence from crustal material (Fig. 8).

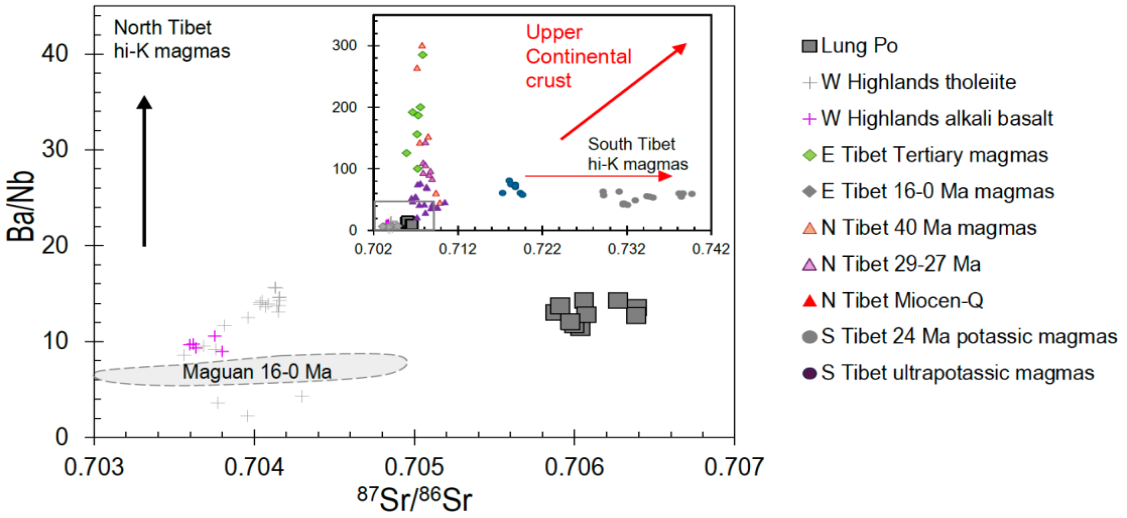

Figure 9. Correlation between $^{87}Sr/^{86}Sr$ and Ba/Nb shows Lung Po and Maguan basalts do not correlate positively with Ba/Nb, suggesting no apparent crustal contamination. In contrast, North Tibet high-K magmas display high Ba/Nb, reflecting the influence of hydrous fluids, while South Tibet magmas with very high $^{87}Sr/^{86}Sr$, suggesting crustal melt influence (inserted diagram). Sources of data fields are as in Fig. 2. See text for explanation

On a Ce/Pb vs. Ce concentration diagram (Fig. 10) the data field of Lung Po basalts plots in the Maguan 12-0 Ma magma's field and almost overlaps that of the representative Vietnam Western Highlands alkaline basalts. They are all embedded in SE I-MORB, defining a mantle-derived magma trend. They plot above a field of arc volcanic rocks, average continental crust (CC), and a bulk earth silicate value (Fig. 10). The North and South Tibet post-collision 42-24 Ma magmas, on the other hand, plot separately to the side of low Ce/Pb ratios and high Ce concentrations, implying significant crustal influence (Rudnick and Fountain, 1995; McLennan, 2001).

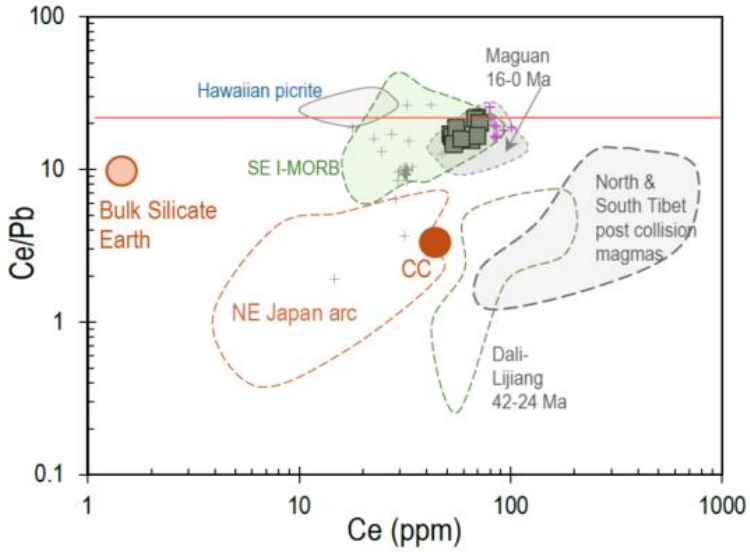

Figure 10. Plots of Ce/Pb vs. Ce for volcanic rocks from various tectonic settings showing Lung Po along with Maguan, Vietnam's Western Highlands, SE I-MORB and Hawaiian (after Norman and Garcia, 1999) magmas plot in the mantle-derived field separated from subduction-related (Kimura and Yoshida, 2006) and crustal related, e.g., Bulk Silicate Earth and Continental Crust (CC) (after Rudnick and Fountain, 1995; McLennan, 2001)

5.2. Asthenosphere or lithospheric mantle sources?

The lithospheric mantle is characterized by its rigidity, coldness, dryness, and refractory nature. Despite these properties, it can produce basaltic melts under elevated temperature conditions, decompression, and hydrous volatiles (e.g., Griffin et al., 2009; see Workman and Hart, 2005). Basalts derived from the lithospheric mantle tend to be relatively depleted in Fe, Ti, Ca, Na, and incompatible elements such as large ion lithophile elements (LILE), high field strength elements (HFSE), and light rare earth elements (LREE). They also show a higher Mg-number for a given MgO content than those derived from fertile mantle sources (Hawkesworth et al., 1993; Turner and Hawkesworth, 1995) (Fig. 11).

Experimental studies on mantle peridotites have shown that, across a range of pressure-temperature (P-T) conditions and degrees of melting, the resulting melts typically contain less than 2.25 wt.% TiO_2 (Hirose and Kushiro, 1993; Kushiro, 1996). Moreover, melting mantle peridotite alone cannot account for high-Ti oceanic island basalt (OIB) (Prytulak and Elliot, 2007). In contrast, melting experiments on mantle garnet pyroxenite produce melts with higher TiO_2 content, reaching up to 2.5 wt.% at 2.5 GPa and 1455°C (Hirschmann et al., 2003). In explaining the isotopic variability in OIB, Prytulak and Elliot (2007) estimate that small amounts (~1–10%) of recycled mafic crust melt incorporated in a mantle peridotite melt can account for all the geochemical constraints, including TiO_2. Since the mafic crust melts at greater depths than the surrounding peridotite, small-degree melts formed beneath the thick lithosphere are more likely to incorporate this enriched material. However, recycled mafic crust may not cover the whole range of isotopic ratios in OIB.

Therefore, subordinated components such as sediments or metasomatic veins are sometimes necessary (Prytulak and Elliot, 2007; e.g., McKenzie et al., 2004).

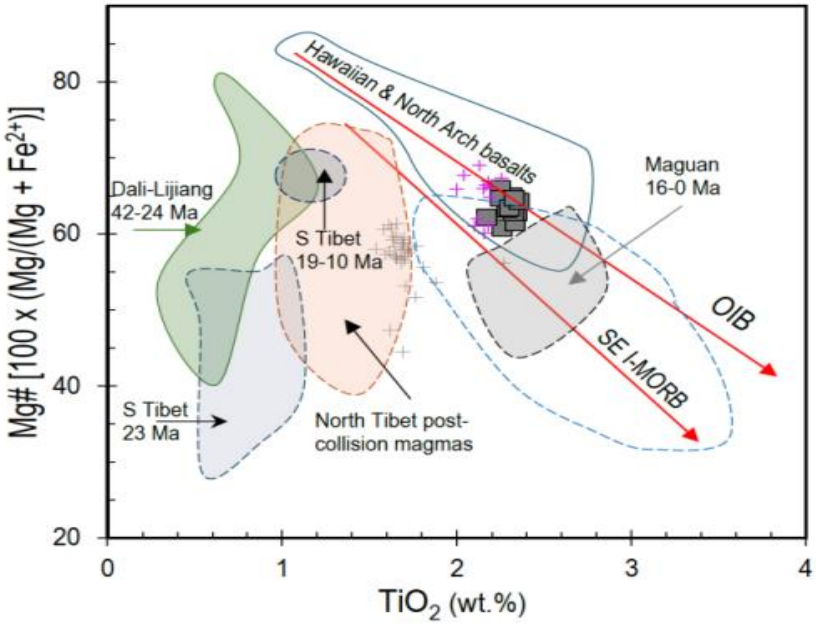

Figure 11. Plots of Mg# [=100 × (Mg/(Mg + Fe^{2+})] vs.TiO_2 shown are fields of crustally influenced North and South Tibet post-collision 42-24 Ma high-K magmas (after Wang et al., 2001; Guo et al., 2006; Liu et al., 2014). Mantle-derived references include SE I-MORB, Hawaiian, and North Arch magmas (Norman and Garcia, 1999; Frey et al., 2000), Lung Po, Maguan, and Vietnam's Western Highlands basalt. See text for explanations

The Lung Po basalts, with high LILE, HFSE, LREE, and TiO_2 contents, are essentially OIB type. This geochemistry means that they are most likely produced by a fertile and enriched asthenosphere source, possibly with the participation of a Ti-rich material.

Wang et al. (2002) compiled geochemical data of basalts from Basin and Range (SW USA), identifying relationships between $Fe_{8.0}$, $[Tb/Yb]_N$, and melting pressure, proposing a line distinguishing garnet- and spinel peridotite melting fields. Furman et al. (2004) applied this model to the East African Rift System (EARS), suggesting that high-Ti magmas with high $[Tb/Yb]_N$ ratios formed with residual garnet, while low-Ti magmas with lower $[Tb/Yb]_N$ ratios formed without it. The Lung Po basalts, aligning with the Vietnam Western Highlands alkaline basalts, fit within the garnet peridotite melting field, with high $[Tb/Yb]_N$ and $[La/Sm]_N$ ratios similar to Ethiopian and Kenyan Rift basalts (Fig. 12).

Flower et al. (2013) examined potassic magmas in the Dali-Lijiang (ca. 40-30 Ma) and Maguan (5-0 Ma) areas, suggesting that older magmas resulted from adiabatic melting of a crustally contaminated asthenosphere, including a hydrated mélange of continental lithospheric mantle (CLM) and delaminated lower crust, enriched by metasomatic melts of subducted continental crust - a mechanism further supported by Zhang et al. (2017). In contrast, the younger intraplate-type basalts and basanites were attributed to

decompression melting of a thermally anomalous, K-rich asthenosphere, which was triggered by regional post-extrusion transtension. This transtension coincided with the cessation of the Indochina escape and adjoining seafloor spreading and was synchronous with widespread intraplate basaltic activity across east and southeast Asia (Flower et al., 2013; e.g., Hoang and Flower, 1998).

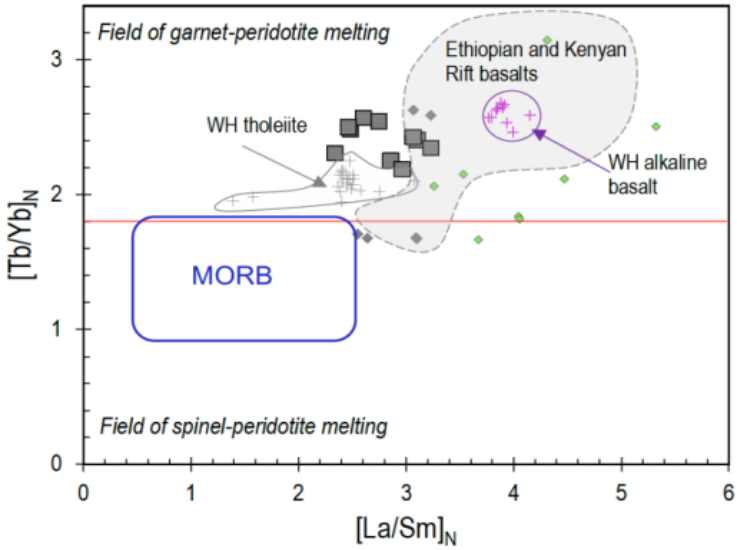

Figure 12. Plots of $[La/Sm]_N$ vs. $[Tb/Yb]_N$ for the Lung Po (filled square) and Maguan 16-0 Ma basalts (gray filled diamond), and 42-24 Ma high-K magmas (green filled diamond) (after Wang et al., 2001). Mantle plume-derived Ethiopian and Kenyan fields are from Furman et al. (2004), Vietnam's Western Highlands (WH) tholeiitic and alkaline basalts are from Hoang et al. (2019). Data for SE Indian MORB are from Neal et al., 2002. In theory, except for the MORB, all the plotted basalts were derived from the field of garnet peridotite melting. Chondrite normalizing data are from Sun and McDonough (1989)

To explain the genesis of the 42-24 Ma Dali-Lijiang potassic magmas, Flower et al. (2013) proposed two models, both of which involve the interaction between delaminated and hydrated continental lithospheric mantle (CLM) and lower crust with convecting asthenosphere, following Indo-Eurasian collision-related processes. This interaction is thought to account for the coexistence of 'enriched' (e.g., potassic and ultrapotassic) and 'depleted' (intraplate type) magmas, a theory supported by tomographic and seismic attenuation investigations in western Yunnan (Liu et al., 2000) and the Vrancea 'bend zone' of the Carpathians (Russo and Mocanu, 2009). Given the nature of Lung Po basalt enrichment and corresponding seismic tomographic evidence under the region (e.g., Phan et al., 2012; Yang et al., 2021; Li et al., 2023; Zhou et al., 2023) it is plausible that similar geodynamic models could explain the Lung Po volcanism.

Further evidence supporting this geodynamic model comes from studying enriched spinel lherzolite xenoliths in Maguan 12-0 Ma alkaline basalts located about 60 km north of Lung Po. These xenoliths, containing more than 15 vol.% clinopyroxene and olivine forsterite up to 90, revealed two-pyroxene geothermometry temperatures from 1029°C to 1148°C. Their spinel-olivine geothermobarometry indicates an oxidation

state from FMQ (fayalite-magnetite-quartz) -1.5 to -0.25, with an average of FMQ -0.59, values comparable to those found in abyssal peridotite and asthenosphere (Xie et al., 2021). Since the Proterozoic subcontinental lithospheric mantle (SCLM) mainly underlies the South China Block, these findings suggest that the ancient refractory lithospheric mantle was replaced by an asthenospheric mantle in localized extensions along the southeastern ASRR shear zone (Wang et al., 2001; Flower et al., 2013; Liu et al., 2013; Xie et al., 2021; e.g., Phan et al., 2012; Li et al., 2023; Zhou et al., 2023).

5.3. The Lung Po basalts' melting depths

Determining the conditions for melt generation requires the chemical composition of the primary melts, which have typically undergone fractional crystallization before eruption. In the Lung Po basalts, olivine is the only phenocryst present (Fig. 2), with the whole rock MgO contents ranging from about 8 wt.% to 10 wt.% and Mg-number [(Mg/(Mg+Fe^{+2})] between 58 to 62. These values are consistent with equilibrium conditions for olivine forsterites with compositions ranging from 81.5 to 84.5, as calculated using a partition coefficient $K_{Fe/Mg}^{ol/liq}$ = 0.30 (e.g., Roeder and Emslie, 1970). These forsterite compositions suggest a moderate degree of olivine fractional crystallization, assuming a maximum olivine forsterite content of 90 (Yamashita and Tatsumi, 1994; Putirka, 2008).

Petrologists have computed primitive melt compositions using the olivine addition method (e.g., Yamashita and Tatsumi, 1994; Putirka, 2008; Hoang et al., 2019). For basalt samples with MgO greater than 8 wt%, there is no evidence of clinopyroxene or plagioclase fractionation, but only olivine. This study applied crystallization modeling using olivine- and glass-based thermometers from Putirka (2008), adding olivine until the final forsterite reached 89-90% and the melt's MgO reached 14-15 wt%, provided these conditions met an equilibrium Fe/Mg partition coefficient of $<0.3 \pm 0.03$ between the whole rock and the olivine phenocryst (see Hoang et al., 2019 for details). The resulting primitive melt compositions are presented in Table 2 and illustrated in Fig. 13.

The relationship between FeO and SiO_2 in computed primitive melts and their erupted counterparts suggests that most tholeiitic basalts from the Vietnam Western Highlands formed within the 10-15 kb range of HK-66 melting, while the corresponding alkaline basalts formed within the 20-25 kb to 30 kbar. Several samples from Lung Po fall within the 15 kbar field while the remainder cluster near the 20-25 kbar field (Fig. 13), indicating that Lung Po basaltic melts were likely produced in the spinel-bearing melting field (Fig. 12) regardless of their trace element characteristics suggesting their generation was in garnet-bearing field (Fig. 12). Robinson and Wood (1998) demonstrated that the spinel-garnet transition in mantle peridotites occurs at about 22 kbar, characterized by 'crossing' REE patterns. However, most Lung Po basalts were generated at pressures lower than 25 kbar, possibly within the spinel or spinel-garnet transition zone rather than in a strictly garnet-bearing melting field (e.g., Robinson and Wood, 1998). This apparent contradiction may be resolved if a high-pressure peridotite body intruded into the shallow mantle, followed by adiabatic decompression melting. However, mixing a small amount of recycled mafic crust melt with a deep-mantle (spinel or garnet) peridotite, as discussed above, could also have produced the Lung Po magmas (e.g., Hirschmann et al., 2003; Prytulak and Elliot, 2007).

Table 2. Chemical compositions of the Lung Po computed primitive melts

Sample	SiO_2	TiO_2	Al_2O_3	Fe_2O_3	FeO	MnO	MgO	CaO	Na_2O	K_2O	P_2O_5	Total
LPO-1	48.92	2.04	10.83	1.43	9.55	0.14	14.02	7.57	2.61	2.45	0.45	100
LPO-2	49.29	1.90	10.52	1.36	9.81	0.13	14.82	6.73	2.64	2.39	0.42	100
LPO-3	47.77	1.95	10.75	1.43	10.11	0.14	15.01	7.23	2.69	2.48	0.45	100
LPO-4	46.92	2.00	10.64	1.42	9.91	0.14	15.04	8.17	2.80	2.45	0.51	100
LPO-5	47.09	1.99	10.56	1.42	9.92	0.14	15.05	8.17	2.65	2.49	0.51	100
LPO-6	48.72	2.02	10.73	1.41	9.51	0.13	14.56	7.42	2.60	2.43	0.45	100
LPO-7	47.16	1.97	10.68	1.42	9.81	0.14	14.79	8.18	2.91	2.44	0.51	100
LPO-8	47.91	2.02	10.91	1.43	9.46	0.15	14.61	8.20	2.30	2.53	0.49	100
LPO-9	49.55	1.99	10.79	1.39	9.38	0.13	14.29	6.98	2.70	2.39	0.42	100
LPO-10	47.43	2.01	10.71	1.42	9.81	0.14	14.84	8.21	2.54	2.41	0.49	100

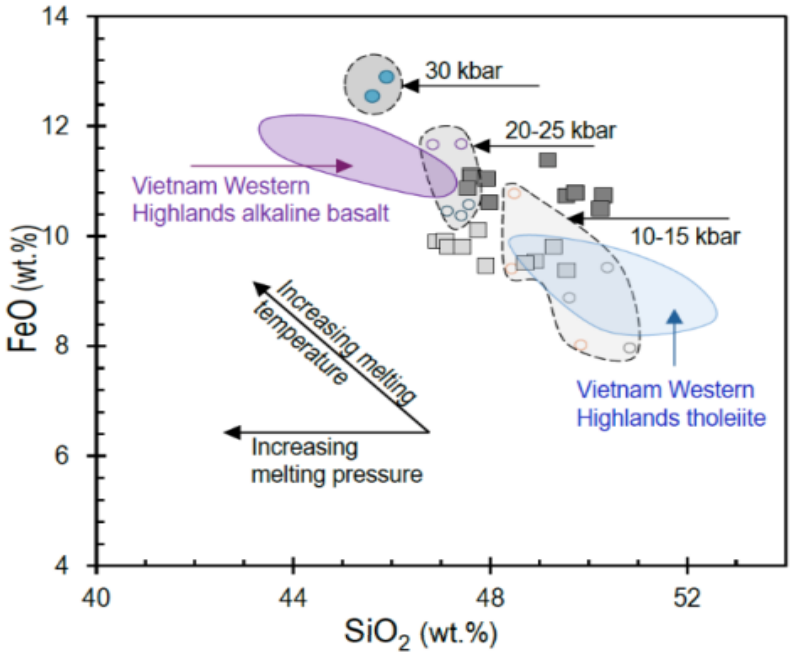

Figure 13. Plots of (wt.%) SiO_2 vs. FeO of the Lung Po basalts (black square) and their primitive melts' chemical compositions (gray square) calculated after Putirka (2008). The experimental peridotite melting pressures of fertile peridotite HK-66 and refractory KBL-1 are after Hirose and Kushiro (1993). Arrows indicate progressive partial melting from low- to high temperature and pressure. Except for a few samples in upper corner of 10-15 kilobars (kb) field, most 'primitive' Lung Po basalts plot in the 20-25 kb field

5.4. The origin of mantle source enrichment beneath the Lung Po area

Elevated strontium (Sr) and lead (Pb), along with lowered neodymium (Nd) isotopic ratios in basaltic rocks compared to typical mantle-derived basalts, suggest multiple origins and evolutionary paths for the basalt. Potential explanations include various scenarios as follows. Basaltic magma may interact with, assimilate, or incorporate enriched components from the continental crust during its ascent. This process often results in higher Sr and Pb isotopic ratios and increased incompatible elements such as Ba, Rb, Th, and U (Zindler and Hart, 1986; Rudnick and Fountain, 1995). During its ascent, the basaltic melt can assimilate older

basaltic material, such as trapped magmatic melts in the subcontinental lithospheric mantle (SCLM) (Carlson and Irving, 1994; Byerly and Lassiter, 2012; Hobbs et al., 2023; Hauzenberger et al., 2024). Ancient geological events can cause specific mantle regions to exhibit distinct isotopic signatures (Hart, 1988; Chavel et al., 1992; Hofmann, 2013). Interactions between basaltic melts and fluids from subducting slabs or sediments can elevate Sr and Pb isotopic ratios and contribute to mantle metasomatism (Tatsumi et al., 2005; Castillo, 2015; Castillo et al., 2018; Zhang et al., 2022).

As discussed in Section 5.1, crustal contamination is considered less likely (Figs. 5a, 9, 10).

5.5. The deep mantle heterogeneity and isotopic mixing

The deep mantle, a crucial part of the Earth's structure, lies beneath the subcontinental lithospheric mantle (SCLM) and extends to the core-mantle boundary. With their consistent trace element patterns and lower concentrations of incompatible elements, rocks from this region provide valuable insights, indicating minimal influence from the crust. The SCLM and deep mantle, despite their proximity, differ significantly in isotopic and trace element compositions, with the deep mantle showing less pronounced variations (Hart, 1988; Stracke et al., 2005; White, 2010; Hofmann, 2013; Tian et al., 2023; Choi et al., 2024; after Zhao et al., 2021).

Various studies suggest a close link between mantle heterogeneity and subducted crustal materials (Hart, 1988; Barling and Goldstein, 1990; Mahoney et al., 2002; Stracke et al., 2005; Hofmann, 2013; Castillo et al., 2018). For instance, Qian et al. (2020) observed that the subducted oceanic lithosphere under the East Vietnam Sea (EVS/SCS) contributes to upper mantle heterogeneity as recycled crustal material (Qian et al., 2020, 2022). Further evidence of regional mantle heterogeneity comes from Tian et al. (2023), who used seismic data to identify reductions in shear velocity due to trapped subducted water and lower continental crust introduced by proto-EVS plate subduction (Tian et al., 2023; after Taylor and Hayes, 1983). The recent development of zinc isotope analysis has further enriched our understanding, offering a valuable method for detecting recycled subducted carbonate in the deep mantle.

The use of Zn isotope to detect recycled sediments in the deep mantle was explained as follows. Carbonates, the primary carbon storage on Earth's surface, can be carried into the mantle through subduction. However, finding evidence of these surface carbonates deep in the mantle has been challenging. Ocean island basalts from the Cook-Austral Islands and St. Helena Island, known as HIMU basalts due to their high uranium-to-lead ratios, are believed to come from mantle plumes originating deep in the lower mantle. The HIMU lavas have unusually high δ^{66}Zn values, higher than most oceanic basalts, indicating that their source includes recycled surface carbonates with heavier isotopes. When the oceanic lithosphere subducts, surface carbonates mix with basaltic crust and melt in the deep mantle, creating carbonatite melts that alter the surrounding mantle. This altered, carbonated mantle eventually forms a high-δ^{66}Zn HIMU source. Thus, the high δ^{66}Zn values in HIMU basalts prove carbonates can be transported deep into Earth's mantle (Zhang et al., 2022; Cao et al., 2024; after Castillo, 2015, and Castillo et al., 2018).

Using the isotopic mixing equation by Langmuir et al. (1978) and geochemical and isotopic data from the literature, mixing between an EM2 and a series of depleted mantle sources (Indian and Pacific MORB-like) may explain the composition of tholeiitic basalts from Vietnam's Western Highlands

(labeled gray cross in Fig. 14) and many post-collision high-K magmas in the ASRRS zone (Line B in Fig. 14). The Lung Po basalt, with high strontium and low coupling neodymium isotopic ratios, shows moderate $^{206}Pb/^{204}Pb$ lead isotopic ratios, ranging from 18.3 to 18.4 (Table 1), plotting outside mixing line B (Fig. 14). To achieve a $^{206}Pb/^{204}Pb$ as low as 18.3, the depleted end member must have a much lower $^{206}Pb/^{204}Pb$ ratio. Therefore, a low-$^{206}Pb/^{204}Pb$ ratio of SE I-MORB is considered as a potential endmember, mixing with another endmember characterized by a $^{206}Pb/^{204}Pb$ ratio as high as 18.45 and an $^{87}Sr/^{86}Sr$ isotopic ratio higher than 0.706 (Line A in Fig. 14).

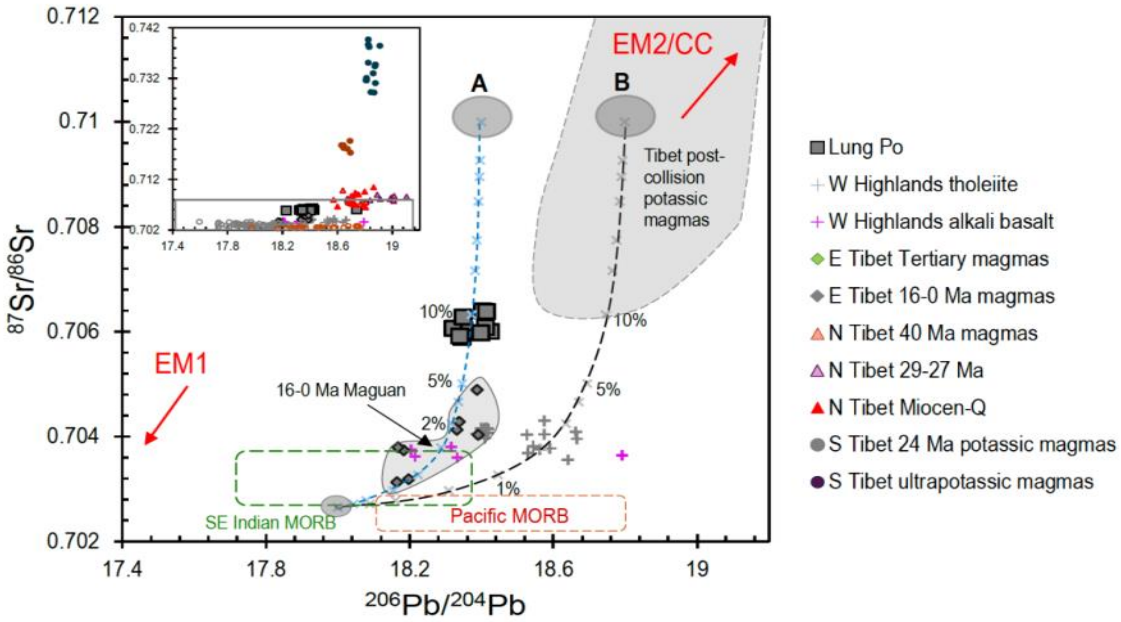

Figure 14. Plots of $^{87}Sr/^{86}Sr$ vs. $^{206}Pb/^{204}Pb$ isotopic mixing model for the Lung Po basalts. The (Pacific or Indian) MORB, for example, serves as a critical endmember. Mixtures of an (N-) MORB with a series of sediments (e.g., Cousens et al., 1994) may explain most high-Pb isotope post-collision 42-24 Ma high-K magmas. However, mixing between a moderate-Pb isotope sediment (e.g., pelagic sediment in the SW sub-basin of EVS/SCS) with a low-Pb isotope Indian (I-) MORB) may explain the formation of the Lung Po and Maguan moderate-Pb and high-Sr isotope samples. Isotopic and elemental values of endmembers used in the mixing model are Pb (ppm), Sr (ppm), $^{206}Pb/^{204}Pb$, and $^{87}Sr/^{86}Sr$, respectively, for an I-MORB-like: 0.2, 25, 18.0, 0.70265; for a SW sub-basin of EVS/SCS: 20, 180, 18.4, and 0.710 (Line A), and a Pacific Ocean-like sediment: 17, 180, 18.8, and 0.710 (Line B). The inserted diagram illustrates the enrichment magnitude of North and South Tibet post-collision high-K magmas. See text for explanations

Since there is no sign of crustal contamination in the Lung Po basalt, the moderate-$^{206}Pb/^{204}Pb$, EM2-like source must be deep-derived, like from a subducted slab extending to the deep mantle (core-inner mantle transition zone?) and later returning to the shallower mantle as recycled crustal materials (Hong-Anh et al., 2018; Zhao et al., 2021; Qian et al., 2022; Tian et al., 2023; Choi et al., 2024). Notably, the relative depletion of U and Th (Fig. 5a) may reflect the presence of recycled crust-derived sediment in the mantle (Kerrich et al., 1999). Crustal sediments in regions like the Pacific

Ocean and the ASRRSZ consistently show high $^{206}Pb/^{204}Pb$ ratios, from 18.6 to 19.2 (Cousens et al., 1994; e.g., Guo et al., 2006; Liu et al., 2014). Thus, an additional subducted source must be considered.

A set of 25 pelagic clays were collected in the SW sub-basin of the EVS at depths from 1,200 to 3,000 m for analysis of Sr, Nd, and Pb isotopic and trace element compositions. The $^{87}Sr/^{86}Sr$ ratios vary between 0.710 and 0.712, and the $^{206}Pb/^{204}Pb$ vary between 18.2 and 18.35, with lead contents varying between 6 and 24 ppm (Hoang N, unpublished data). If this type of sediment were introduced into the mantle by a subducted slab, about 10% of the sediment mixing with an (SE) I-MORB-like melt would produce the Lung Po isotope with a moderate-lead ratio (Line A, Fig. 14).

Previous studies have explored the origins of regional post-collision volcanic rocks, revealing intermittent occurrences around 45-38 Ma, 30-24 Ma, and from 18 (or 16) Ma to the present in northern and southern Tibet and the ASRRSZ areas. Magmas in northern Tibet originated from an enriched asthenospheric source combined with crustal assimilation and metasomatized continental lithosphere, resulting from subducted sediments following the India-Eurasia collision (Zhang and Schärer, 1999; Guo et al., 2006; Zhang et al., 2017). In contrast, potassic volcanic rocks in southern Tibet were produced by a hydrous lithospheric mantle that underwent multiple metasomatic events during the Neo-Tethys oceanic subduction, incorporating lower crust and ancient Lhasa basement rocks (Liu et al., 2014) (Figs. 6-7, 9-11, 14). Furthermore, extensional tectonics and thickened crust facilitated early Miocene magmatism along major regional strike-slip faults. Later (12-0 Ma) magmas were produced by decompression melting of a metasomatically altered, newly emplaced asthenospheric mantle following local lithospheric extension and delamination (e.g., Wang et al., 2001; Flower et al., 2013; Liu et al., 2014; Xie et al., 2021).

Notably, the 12-0 Ma Maguan alkaline basalt, about 65 km north of Lung Po, plots almost along Line A (Fig. 14). Mixing from 1 to 5% of the sediment with the SE I-MORB melt would explain the isotopic range of the basalt. This observation suggests that the asthenospheric mantle source in southeastern ASRR shear zone is heterogeneous both spatially and temporally (e.g., Wang et al., 2001; Flower et al., 2013; Xie et al., 2021; this study).

6. Conclusions

(i) The Lung Po olivine-phyric alkaline basalt is approximately 1 km² in northern Bat Xat District (Lao Cai province, Northern Vietnam). It is dated between 0.9 and 0.5 Ma. This basaltic outcrop is about 12 km west of the ASRRS zone's axis and roughly 65 km south of the post-India-Eurasian collision (12-0 Ma) Maguan mantle xenolith-bearing alkaline basalt in southwest Yunnan, China, within the ASRRS zone. The geochemical compositions of these basalts differ significantly from the early 42-24 Ma high-K magmatic rocks. They display oceanic island basalt trace element distribution patterns and more depleted radiogenic isotopic compositions.

(ii) The early volcanic stage in the ASRRSZ (42-24 Ma) was associated with crustal tectonics, while mantle dynamics governed the later stage (12-0 Ma or 16-0 Ma). The Lung Po and 12-0 Ma Maguan alkaline basalt were produced by decompression melting of a relatively depleted asthenospheric mantle, which replaced the lithospheric mantle following localized extension and lower crust delamination.

(iii) Interpretation of the computed primitive melt compositions of Lung Po reveals that they were generated under

pressures ranging from 15 to 25 kb (approximately 45 to 75 km deep), possibly in the spinel or garnet-spinel peridotite transition melting field, with $[Tb/Yb]_N$ between 2.2 and 2.6 and $[La/Sm]_N$ from 2 to 3.

(iv) The high $^{87}Sr/^{86}Sr$ ratios, coupled with low $^{143}Nd/^{144}Nd$, moderate $^{176}Hf/^{177}Hf$, and $^{206}Pb/^{204}Pb$ isotopic ratios in the Lung Po basalt, suggest mixing between low-lead isotope Indian MORB and a moderate-lead isotope crustal source introduced by a subducted slab to the deep-level mantle, later returning to the shallower mantle as recycled crustal materials. Although the isotopic compositions of the 12-0 Ma Maguan basalt differ from those of the Lung Po, they plot on the same isotopic mixing curve, indicating they may share the same mixing sources but in different proportions. This observation suggests temporal and spatial heterogeneity in the asthenosphere beneath the southeastern ASRR shear zone.

Acknowledgments

We thank Zoltán Pécskay for kindly assisting in K-Ar age dating and Le Duc Anh for patiently computing the primitive melt compositions. We are grateful to Pham Thi Dung (IGS, VAST) for generously providing us with travel support for the first field trip to the Lung Po basaltic outcrop. This study is financed by the Institute of Geological Sciences selective basic project CSCL11.01/23-24 and by the Vietnam Academy of Science and Technology research project VAST05.01/23-24, to whom the authors gratefully acknowledge. Two anonymous reviewers' critical and thoughtful comments and suggestions helped clarify and significantly improve the manuscript from an early version. The authors are deeply grateful for their time and patience.

References

Balogh K., 1985. K/Ar dating of Neogene volcanic activity in Hungary: Experimental technique, experiences and methods of chronologic studies. ATOMKI Rep. D/1., 277–288.

Balogh K., Árva-Sós E., Pécskay Z., Ravasz-Baranyai L., 1986. K/Ar dating of Post-Sarmatian alkali basaltic rocks in Hungary. Acta Mineralogica-Petrographica, Szeged 28 (1986)75. ATOMKI ref. code: P05944.

Barling J., Goldstein S.L., 1990. Extreme isotopic variations in Heard Island lavas and the nature of mantle reservoir. Nature, 348, 59–62.

Bouvier A., Vervoort J.D., Patchett P.J., 2008. The Lu–Hf and Sm-Nd isotopic composition of CHUR: Constraints from unequilibrated chondrites and implications for the bulk composition of terrestrial planets. Earth Planet Sci. Lett., 273(1–2), 48–57.

Briais A., Patriat P., Tapponnier P., 1993. Updated interpretation of magnetic anomalies and seafloor spreading stages in the South China Sea (East Sea), implications for the Tertiary tectonics of SE Asia. Journal Geophysical Research, 98, 6299–6328.

Byerly B.L., Lassiter J.C., 2012. Evidence from mantle xenoliths for lithosphere removal beneath the central Rio Grande Rift. Earth and Planetary Science Letters, 355–356, 82–93. https://doi.org/10.1016/j.epsl.2012.08.034.

Cao G., Tong Y., Tang X-Ch., Wang X-D., Li X., Wang L., 2024. Deep recycling of crustal materials by the Hainan mantle plume: evidence from Zn-Sr-Nd-Pb isotopes of Hainan Island basalts. Contributions to Mineralogy and Petrology, 179, 30.

Carlson R.W., Irving A.J., 1994. Depletion and enrichment history of subcontinental lithospheric mantle, An Os, Sr, Nd, and Pb isotopic study of ultramafic xenoliths from northern Wyoming Craton. Earth Planet Sci Lett, 126, 457–472.

Castillo P.R., 2015. The recycling of marine carbonates and sources of HIMU and FOZO ocean island basalts. Lithos, 216–217, 254–263.

Castillo P.R., MacIsaac C., Perry S., Veizer J., 2018. Marine carbonates in the mantle source of oceanic basalts: Pb isotopic constraints. Scientific Reports, 8, 14932. Doi: 10.1038/s41598-018-33178-4.

Chavel C., Hofmann A.W., Vidal P., 1992. HIMU-EM1: the French Polynesian connection. Earth and Planetary Science Letters, 110, 99–119.

Choi S.H., Hong-Anh H.T., Liu Sh-A., 2024. Zinc isotopic compositions of late Cenozoic basaltic rocks from Vietnam: Constraints on recycled carbonates in the mantle source. Journal of Asian Earth Sciences, 264, 106039.

Chung S.L., Lee T.Y., Lo C.H., Wang P.L., Chen C.Y., Nguyen T.Y., Tran T.H., Wu G.Y., 1997. Intraplate extension prior to continental extrusion along the Ailao Shan-Red River shear zone. Geology, 25(4), 311–314.

Cox A., Dalrymple G.B., 1967, Geomagnetic polarity epochs; Nunivak Island, Alaska: Earth and Planetary Science Letters, 3, 173–177.

DePaolo D.J., Wasserburg G.J., 1976. Nd isotopic variations and petrogenetic models. https://doi.org/10.1029/GL003i005p00249.

Flower M.F.J., Hoang N., Lo Ch-h, Cung T.C., Nguyen Q.C., Liu F-t., Deng J-f., Mo X-x., 2013. Potassic magma genesis and the Ailao Shan-Red River fault. Journal Geodynamics, 69, 84–105.

Frey F.A., Clague D., Mahoney J.J., Sinton J.M., 2000. Volcanism at the edge of the Hawaiian plume: petrogenesis of submarine alkalic lavas from the North Arch volcanic field. Journal of Petrology, 41(5), 667–691.

Furman T., Bryce J.G., Karson J., Iotti A., 2004. East African Rift system (EARS) plume structure: Insights from Quaternary mafic lavas of Turkana, Kenya. Journal of Petrology, 45(5), 1069–1088. Doi: 10.1093/petrology/egh004.

Gill J.B., 1981. Orogenic andesite and plate tectonics. Springer-Verlag, New York, 330p.

Griffin W.L., O'Reilly S.Y., Afonso J.C., Begg G.C., 2009. The composition and evolution of lithospheric mantle: a re-evaluation and its tectonic implications. Journal of Petrology, 50(7), 1185–1204.

Guo Z., Wilson M., Liu J., Mao Q., 2006. Post-collisional, potassic and ultrapotassic magmatism of the Northern Tibetan Plateau: Constraints on characteristics of the mantle source, geodynamic setting and uplift mechanisms. Journal of Petrology, 47(6), 117–1220. Doi: 10.1093/petrology/egl007.

Harrison T.M., Leloup P.H., Ryerson F.J., Tapponnier P., Lacassin R., Chen W., 1996. Diachronous initiation of transtension along the Ailao Shan-Red River Shear Zone, Yunnan and Vietnam. Tectonic evolution of Asia. World and regional geology series. New York, Cambridge University Press, 208–226.

Hart S., 1988. Heterogeneous mantle domains: signatures, genesis and mixing chronologies. Earth and Planetary Science Letters, 90, 273–296.

Hart S.R., 1984. A large-scale isotopic anomaly in the Southern Hemisphere. Nature, 309, 753–757.

Hauzenberger C.A., Konzett J., Joachim-Mrosko B., Hoang N., 2024. Pliocene to Pleistocene REE-P metasomatism in the subcontinental lithosphere beneath south Asia - evidence from a monazite and REE-rich apatite-bearing peridotite xenolith from central Vietnam. Journal of Petrology. Doi/10.1093/petrology/egae015/7612967.

Hawkesworth C.J., Gallagher K., Hergt J.M., McDermott F., 1993. Mantle and slab contributions in arc magmas. Annual Review of Earth and Planetary Sciences, 21, 175–204.

He Q., Xiao L., Balta B., Gao R., Chen J., 2010. Variety and complexity of the Late-Permian Emeishan basalts: reappraisal of plume-lithosphere interaction processes. Lithos, 119, 91–107. Doi: 10.1016/j.lithos.2010.07.020.

Hirose K., Kushiro I., 1993. Partial melting of dry peridotites at high pressures: determination of composition of melts segregated from peridotite using aggregate of diamond. Earth and Planetary Science Letters, 114, 477–489.

Hirschmann M.M., Kogiso T., Baker M.B., Stolper E.M., 2003. Alkalic magmas generated by partial melting of garnet pyroxenite. Geology, 31(6), 481–484.

Hoang N., Flower M.F.J., 1998. Petrogenesis of Cenozoic basalts from Vietnam: implication for origins of a 'diffuse igneous province'. Journal of Petrology, 39(3), 369–395. https://doi.org/10.1093/petroj/39.3.369.

Hoang N., Flower M.F.J., Carlson R.W., 1996. Major, trace element, and isotopic compositions of Vietnamese basalts: interaction of hydrous EM1-rich

asthenosphere with thinned Eurasian lithosphere. Geochimica et Cosmochimica Acta, 60, 4329–4351.

Hoang N., Ogasawara M., Tran T.H., Phan V.H., Nguyen T.T., Cu S.T., Pham T.D., Pham T.X., 2014. Geochemistry of Neogene basalts in the Nghia Dan district, western Nghe An. Vietnam Journal of Earth Sciences, 36(4), 403–412. https://doi.org/10.15625/0866-7187/36/4/6428.

Hoang N., Shinjo R., La T.P., Le Duc Anh, Tran Thi Huong, Zoltán Pécskay, Dao Thai Bac, 2019. Pleistocene basalt volcanism in the Krông Nô area and vicinity, Dak Nong province (Vietnam). J. Asian Earth Sciences, 181, 103903.

Hobbs K.P., Elkins L.J., Lassiter J.C., Hoang N., Burberry C.M., 2023. Characterizing peridotite xenoliths from southern Vietnam: Insight into the underlying lithospheric mantle. Geochemistry, Geophysics, Geosystems, 24(7), e2023GC010971. https://doi.org/10.1029/2023GC010971.

Hofmann A.W., 2013. Sampling mantle heterogeneity through oceanic basalts: Isotopes and trace elements In: Turekian, K., Holland, H. (Eds) Treatise in Geochemistry, Elsevier. Amsterdam, 67–101.

Hong-Anh H.T., Choi S.H., Yu Y-j, Pham T.H., Nguyen K.H., Ryu J.-S., 2018. Geochemical constraints on the spatial distribution of recycled oceanic crust in the mantle source of late Cenozoic basalts. Vietnam. Lithos, 296–299, 382–395.

Huong T.T., Hoang N., 2018. Petrology, geochemistry, and Sr, Nd isotopes of mantle xenolith in Nghia Dan alkaline basalt (West Nghe An): implications for lithospheric mantle characteristics beneath the region. Vietnam Journal of Earth Sciences, 49(3), 207–227. Doi: 10.15625/0866-7187/40/3/12614.

Johnson K.T.M., Dick H.J.B., Shimizu N., 1990. Melting in the oceanic upper mantle: An ion microprobe study of diopsides in abyssal peridotites. Journal of Geophysical Research, 95, 2661–2678.

Jones R.E., van Keken P.E., Hauri E.H., Tucker J.M., Vervoort J., Ballentine C.J., 2019. Origins of the terrestrial Hf-Nd mantle array: Evidence from a combined geodynamical-geochemical approach. Earth Planet Sci. Lett., 518, 26–39.

Kerrich R., Wyman D., Hollings P., Polat A.,1999. Variability of Nb/U and Th/La in 3.0–2.7Ga Superior province ocean plateau basalts: Implications for the timing of continental growth and lithosphere recycling. Earth and Planetary Science Letters, 168, 101–115.

Kimura J.-I., Yoshida T., 2006. Contributions of slab fluid, mantle wedge and crust to the origin of Quaternary lavas in the NE Japan arc. Journal of Petrology, 47(11), 2185–2232.

Koszowska E., Wolska A., Zuchiewicz W., Nguyen Q.C., Pecskay Z., 2007. Crustal contamination of Late Neogene basalts in the Dien Bien Phu Basin, NW Vietnam: Some insights from petrological and geochronological studies. Journal of Asian Earth Sciences, 29, 1–17.

Kushiro I., 1996. Partial melting of a fertile mantle peridotite at high pressure: An experimental study using aggregates of diamond. In: Basu A., Hart SR (eds) Earth Processes, Reading the Isotopic Code. Geophysical Monograph. American Geophysical Union, Washington, D.C., 95, 109–122.

Langmuir C.H., Vocke R.D., Hanson G.N., 1978. A general mixing equation with application to Icelandic basalts. Earth and Planetary Science Letters, 37, 380–392.

Le Bas M.J., Le Maitre R.W., Streckeisen A., Zanettin B., 1986. A Chemical Classification of Volcanic Rocks Based on the Total Alkali-Silica Diagram. Journal of Petrology, 27, 745–750.

Leloup P.H., Arnau N., Lacassin R., Kienast J.R., Harrison T.M., Phan Trong Trinh, Replumaz A., Tapponnier P., 2001. New constraints on the structure, thermochronology and timing of the Ailao Shan-Red River shear zone, SE Asia. Journal of Geophysical Research, 106, 6657–6671.

Li L., Lu S-P., Gao L., Lei C., 2023. Seismic reflection imaging of a deep-penetrating Red River Fault in the Yinggehai Basin, northwest of the South China Sea (East Sea). Geophysical Research Letters, 50, e2023GL104598. https://doi.org/10.1029/2023GL104598.

Liu C.Z., Wu F.Y., Sun J., Chu Z.Y., Yu X.H., 2013. Petrology, geochemistry and Re–Os isotopes of peridotite xenoliths from Maguan, Yunnan Province: implications for the Cenozoic mantle replacement in southwestern China. Lithos, 168–169, 1–14.

Liu D., Zhao Z., Zhu D-Ch., Niu Y., DePaolo D.J., T. Harrison M., Mo X-x., Dong G., Zhou S., Sun C., Zhang Z., Liu J., 2014. Postcollisional potassic and

ultrapotassic rocks in southern Tibet: Mantle and crustal origins in response to India-Asia collision and convergence. Geochimica et Cosmochimica Acta, 143, 207–231. https://doi.org/10.1016/j.gca.2014.03.031.

Liu F., Liu J., Zhong D., He J., You Q., 2000. The subducted slab of Yangtze continental block beneath the Tethyan orogen in western Yunnan. Chinese Science Bulletin, 45(5), 466–472.

Mahoney J.J, Graham D.W., Christie D.M., Johnson K.T.M., Hall S.L., Vonderhaar D.L., 2002. Between a hotspot and a cold spot: Isotopic variation in the Southeast Indian Ridge asthenosphere, 86E-118E. Journal of Petrology, 43(7), 1155–1176.

Maluski H., L.C. Jolivet, L. Carter, A. Roques, D. Beyssac O., Ta Trong Thang, Nguyen Duc T., Avigad D., 2001. Ar-Ar and fission track ages in the Song Chay massif: Early Triassic and Cenozoic tectonics in northern Vietnam. Journal of Asian Earth Sciences, 19, 233–248.

McKenzie D., Stracke A., Blichert-Toft J., Albarède F., Grönvold K., O'Nions R.K., 2004. Source enrichment processes responsible for isotopic anomalies in oceanic island basalts. Geochimica et Cosmochimica Acta, 68(12), 2699–2724.

McLennan S.M., 2001. Relationships between the trace element composition of sedimentary rocks and upper continental crust. Geochemistry, Geophysics, Geosystems, 2, 2000GC000109.

Neal C.R., Mahoney J.J., Chazey III W.J., 2002. Mantle sources and the highly variable role of continental lithosphere in basalt petrogenesis of the Kerguelen Plateau and Broken Ridge LIP: Results from ODP Leg 183. J. Petrol, 43(7), 1177–1205.

Norman M.D., Garcia M.O., 1999. Primitive magmas and source characteristics of the Hawaiian plume: petrology and geochemistry of shield picrites. Earth and Planetary Science Letters, 168, 27–44.

Pham T.D., Usuki T., Tran T.H., Hoang N., Usuki M., Pham M., Nong T.Q.A., Nguyen V.Y., Pham T.H., 2023. Emplacement ages, geochemical and Sr-Nd-Hf isotopic characteristics of Cenozoic granites in the Phan Si Pan uplift, Northwestern Vietnam: petrogenesis and tectonic implication for the adjacent structure of the Red River shear zone. International Journal of Earth Sciences, 112, 1475–1497. https://doi.org/10.1007/s00531-023-02307-4.

Phan T.T., Ngo V.L., Nguyen V.H., Hoang Q.V., Bui V.T., Bui P.T., Mai T.T., Hoang N., 2012. Late Quaternary tectonics and seismotectonics along the Red River fault zone, North Vietnam. Earth-Science Reviews, 114 (3–4), 224–235.

Prytulak J., Elliot T., 2007. TiO_2 enrichment in ocean island basalts. Earth Planet Sci. Lett., 263 (3–4), 388–403.

Putirka K., 2008. Thermometers and Barometers for Volcanic Systems. In: Putirka, K., Tepley, F. (Eds.), Minerals, Inclusions and Volcanic Processes, Reviews in Mineralogy and Geochemistry, Mineralogical Soc. Am., 69, 61–120.

Qian S., Salters V.J., McCoy-West A.J., Wu J., Rose-Koga E.F., Nichols A.R.L., Zhang L., Zhou H-Y., Hoernle K., 2022. Highly heterogeneous mantle caused by recycling of oceanic lithosphere from the mantle transition zone. Earth and Planetary Science Letters, 593, 117670.

Qian S.-P., Zhou H., Zhang L., Cheng R., 2020. Mantle heterogeneity beneath the South China Sea (East Sea): Chemical and isotopic evidence for contamination of ambient asthenospheric mantle. Lithos, 354–355.

Qiao L., Yao H., Lai Ya-Ch., Huang Bor-Sh., Zhang P., 2018. Crustal structure of southwest China and northern Vietnam from ambient noise tomography: Implication for the large-scale material transport model in SE Tibet. Tectonics, 37. https://doi.org/10.1029/2018TC004957.

Ringwood A.E., 1966. The Chemical Composition and Origin of the Earth. In: Hurley, P.M., Ed., Advances in Earth Science, M.I.T. Press, Cambridge, MA, 287–356.

Robinson J.A., Wood B.J., 1998. The depth of the spinel to garnet transition at the peridotite solidus. Earth Planet. Sci. Lett., 164, 277–284.

Roeder P.L., Emslie R.F., 1970. Olivine-liquid equilibria. Contribution to Mineralogy and Petrology, 29, 275–289.

Rudnick R.L., Fountain D.M., 1995. Nature and composition of the continental crust: a lower crustal

perspective. Reviews of Geophysics, 33(3), 267–309.

Russo R.M., Mocanu V.I., 2009. Source-side shear wave splitting and upper mantle flow in the Romanian Carpathians and surroundings. Earth and Planetary Science Letters 287(1–2), 205–216.

Shinjo R., Ginoza Y., Meshesha D., 2010. Improved method for Hf separation from silicate rocks for isotopic analysis using Ln-spec resin column. J. Mineral. Petrol. Sci., 105, 297–302.

Steiger R.H., Jäger E., 1977. Subcommission on geochronology: Convention on the use of decay constants in geo- and cosmochronology. Earth and Planetary Science Letters, 36(3), 359–362.

Stracke A., Hofmann A.W., Hart S.R., 2005. FOZO, HIMU, and the rest of the zoo. Geochemistry, Geophysics, Geosystems, 6(5). doi.org/10.1029/2004GC000824.

Sun S.-S., McDonough W.F., 1989. Chemical and isotope systematics of mid-ocean ridge basalts: implications for mantle composition and processes. In: A.D. Sander and M.J. Norry (Editors), Magmatism in the Ocean Basin. Geological Society of London Special Publication, 313–345.

Tapponnier P., Lacassin R., Leloup P.H., Shärer U., Dalai Z., Haiwei W., Xiaohan L., Shaocheng J., Lianshang Z., Jiayou Z., 1990. The Ailao Shan/Red River metamorphic belt: Tertiary left-lateral shear between Indochina and South China. Nature, 343(6257), 431–437. http://dx.doi.org/10.1038/343431a0.

Tapponnier P., Peltzer G., Le Dain A.Y., Armijo R., Cobbold P., 1982. Propagating extrusion tectonics in Asia: New insights from simple experiments with plasticine. Geology, 7, 611–616.

Tatsumi Y., Shukuno H., Yoshikawa M., Chang Q., Sato K., Lee M.W., 2005. The petrology and geochemistry of volcanic rocks on Jeju Island: Plume magmatism along the Asian continental margin. Journal of Petrology, 46(3), 523–553. Doi: 10.1093/petrology/egh087.

Tatsumoto M., Basu A.R., Huang W., Wang J., Xie G., 1992. Sr, Nd, and Pb isotopes of ultramafic xenoliths in volcanic rocks of eastern China: enriched components EMI and EMII in subcontinental lithosphere. Earth and Planetary Science Letters, 113, 107–128.

Tatsumoto M., Nakamura Y., 1991. DUPAL anomaly in the Sea of Japan: Pb, Nd and Sr isotopic variations at the eastern Eurasian continental margin. Geochimica et Cosmochimica Acta, 55, 3697–3708.

Taylor B., Hayes D.E., 1983. Origin and history of the South China Sea (East Sea) basin. In Hayes, D.E. (Ed.), The Tectonic and Geologic Evolution of Southeast Asian Seas and Islands (Pt. 2). Geophysical Monograph, 27, 23–56.

Tian J., Ma Z., Lin J., Xu M., Yu X., Le Ba Manh, Zhang X., Zhang F., Guo L., 2023. Mantle heterogeneity caused by trapped water in the Southwest basin of the South China Sea (East Sea). Nature Communications, 14, 2710. doi.org/10.1038/s41467-023-38385-w.

Tran T.H., Polyakov A.S., Izokh A.E., Balykin P.A., Ngo T.P., Pham T.D., 2016. Intraplate magmatism and metallogeny of North Vietnam. Modern approaches in Solid Earth Sciences. Springer Switzerland, 11, 332. Doi: 10.1007/978-3-319-25235-3.

Tu K., Flower M.F.J., Carlson R.W., Zhang M., Xie G.-H., 1991. Sr, Nd, and Pb isotopic compositions of Hainan basalts (south China), implications for a subcontinental lithosphere Dupal source. Geology, 19, 567–569.

Turner S., Hawkesworth C., 1995. The nature of the sub-continental mantle, constraints from the major element composition of continental flood basalts. Chemical Geology, 120, 295–314.

Wang J-H., Yin A., Harrison T.M., Grove M., Zhang Y-Q., Xie G-H., 2001. A tectonic model for Cenozoic igneous activities in the eastern Indo-Asian collision zone. Earth and Planetary Science Letters, 188, 123–133.

Wang K., Plank T., Walker J.D., Smith E.I., 2002. A mantle melting profile across the Basin and Range, SW USA. Journal of Geophysical Research, 107, 10.1029/2001JB000209.

White W.M., Hofmann A.W., Puchelt H., 1987. Isotope geochemistry of Pacific mid-ocean ridge basalt. Journal of Geophysical Research, 92(B6), 4881–4893.

Wiedenbeck M., Alle´ P., Corfu F., Griffin W.L., Meier M., Oberli F., Von Quadt A., Roddick J.C., Spiegel W., 1995. Three natural zircon standards for U-Th-

Pb, Lu-Hf, trace element and REE analyses. Geostand. Newsl, 19, 1–23.

Workman R.K., Hart S.R., 2005. Major and trace element composition of the depleted MORB mantle (DMM). Earth and Planetary Science Letters, 231(1–2), 53–72.

Xie Z., Hattori K., Wang R., Wang J., Jiao Q-q., Wang D., 2021. Evolution of lithospheric mantle beneath the Maguan region, southwestern margin of the South China block based on mantle xenoliths in Miocene alkaline volcanic rocks. Mineralogy and Petrology, 115, 173–192. https://doi.org/10.1007/s00710-021-00739-x.

Yamashita S., Tatsumi Y., 1994. Thermal and geochemical evolution of the mantle wedge in the northeast Japan arc. 2. Contribution from geochemistry. Journal of Geophysical Research, 99, 22, 285–222,293.

Yang X., Yao H., Huang B.-S., 2021. Crustal footprint of mantle upwelling and plate amalgamation revealed by ambient noise tomography in northern Vietnam and the northern South China Sea (East Sea). Journal of Geophysical Research: Solid Earth, 126, e2020JB020593. https://doi.org/10.1029/2020JB020593.

Zhang G-L., Luo Q., Zhao J., Jackson M.G., Guo L-S., 2018. Geochemical nature of sub-ridge mantle and opening dynamics of the South China Sea (East Sea). Earth and Planetary Science Letters, 489, 145–155.

Zhang L., Guo Z., Zhang M., Cheng Z., Sun Y., 2017. Post-collision potassic magmatism in the eastern Lhasa terrane, South Tibet: Products of partial melting of mélanges in a continental subduction channel. Gondwana Research, 41, 9–28.

Zhang L-Sh., Schärer U., 1999. Age and origin of magmatism along the Cenozoic Red River shear belt, China. Contribution to Mineralogy and Petrology, 134, 67–85.

Zhang X-Y., Chen L-H., Wang X-J., Hanyu T., Hofmann A.W., Komiya T., Nakamura K., Kato Y., Zeng G., Gou W-X., Li W-Q., 2022. Zinc isotopic evidence for recycled carbonate in the deep mantle. Nature Communications, 13, 6085. doi.org/10.1038/s41467-022-33789-6.

Zhao D., Toyokuni G., Kurata K., 2021. Deep mantle structure and origin of Cenozoic intraplate volcanoes in Indochina, Hainan and South China Sea (East Sea). Geophysical Journal International, 225, 572–588.

Zhou Q., Li X., Chang Y., Yu J., Luo W., Bai X., 2023. Strong earthquake recurrence interval in the southern segment of the Red River Fault, southwestern China. Frontiers in Earth Science, 11, 1280787. Doi: 10.3389/feart.2023.1280787.

Zindler A., Hart S., 1986. Chemical Geodynamics. Annual Review of Earth and Planetary Sciences, 14, 493–571.